Relationship between microstructure and strain-hardening behaviour of 3D printed engineered cementitious composites

Binrong Zhu[a,b], Jinlong Pan[a,*], Junrui Li[a], Penghui Wang[c], Mingzhong Zhang[b,**]

[a]Key Laboratory of Concrete and Prestressed Concrete Structures of Ministry of Education, School of Civil Engineering, Southeast University, Nanjing, 211189, China

[b]Department of Civil, Environmental and Geomatic Engineering, University College London, London, WC1E 6BT, UK

[c]College of Civil and Transportation Engineering, Shenzhen University, Shenzhen, 518060, China

Abstract: The tensile behaviour of engineered cementitious composites (ECC) is highly dependent on their microstructure characteristics. To date, the strain-hardening behaviour of printed ECC in relation to its microstructure is not yet fully understood. This study presents a systematic investigation on the macroscopic mechanical properties of normal and printed ECC with various polyethylene (PE) fibre lengths (6 and 12 mm) in relation to their microstructural features in terms of pore structure characteristics, fibre orientation and fibre dispersion through a series of mechanical tests and X-ray computed tomography (CT) and backscattered electron (BSE) image acquisition, processing and analysis. Results indicate that it is desirable to use block specimens for mould-casting fabrication as contrast to printed ECC samples. The printed ECC containing 1.5 vol% 6 mm and 0.5 vol% 12 mm PE fibres by extrusion-based 3D printing exhibits unique tensile ductility of over 5% and average crack width of less than 100 μm. Regarding pore structure, normal ECC has a higher probability of large pores (over 1 mm^3) than printed ECC, which would increase the risk of damage localization and lead to a significant variation in tensile properties. Besides, normal ECC with thickness of 30 mm and printed ECC possess a similar fist cracking strength as indicated by similar pore size and fracture toughness. Compared to normal ECC, printed ECC has a more uniform dispersion of PE fibres, the orientation of which is more perpendicular to the loading direction, resulting in a higher average tensile strength and strain capacity than normal ECC.

Keywords: 3D concrete printing; Strain-hardening cementitious composites; Tensile properties; Microcracking; Fibre bridging effect; Pore structure

1. Introduction

3D concrete printing (3DCP) is an emerging additive manufacturing technology to create individualized objects layer by layer without human intervention and formwork [1, 2]. With the rapid development of 3D printing technology, it has been increasingly applied in the construction industry. Three different additive manufacturing techniques including particle-bed binding (or powder-based 3D printing), material jetting (or shotcrete 3D printing) and extrusion-based 3D printing were

* Corresponding author. E-mail address: cejlpan@seu.edu.cn (J. Pan).

** Corresponding author. E-mail address: mingzhong.zhang@ucl.ac.uk (M. Zhang).

developed for 3DCP, among which extrusion-based 3DCP is most widely adopted in the construction industry [3, 4]. In recent years, some large-scale 3D printed concrete structural elements or structures including complex hollow concrete columns [5], concrete bathroom unit [6], and beam and arch bridges [7-11] were produced for demonstration purposes, which have received a lot of attention and interests.

To ensure the mechanical performance and integrity of printed concrete structures, reinforcement is required, while how to incorporate reinforcement in 3DCP is still a major challenge. Over the past few years, a few structural reinforcing methods have been proposed to incorporate the reinforcement during the extrusion-based 3DCP process including automated entrainment of continuous reinforcement microcable [12-14] or continuous fibre [15-17] in the filament, bar-penetrated reinforcement with lap joints or concurrent deposition of U-nails to strengthen the interface bonding [18-21], and short-fibre reinforcement for self-reinforced cementitious composites [22-25]. Compared to the former two reinforcement approaches, 3D printing process with dispersed short fibres is more compatible with 3DCP process in the view of the ability for streamlined integration in practice as it does not require special-designed equipment or any further extra process for reinforcement integration. A combination of 3D printing technology with ECC offers opportunities to significantly reduce or even eliminate the reinforcement usage of the resulting structure in the print plane [26-28]. As a special class of fibre reinforced cementitious composites designed and tailored based on micromechanics theory, engineered cementitious composites (ECC), also known as strain-hardening cementitious composites (SHCC) or bendable concrete has been widely used in civil infrastructures such as buildings, bridges, water and energy infrastructures, tunnels and so on [29-33]. The tensile strain capacity of ECC with 2 vol% of fibres is typically over 2% or 200 times that of normal concrete or ordinary fibre reinforced concrete (FRC) [34]. Unlike the common FRC that exhibits tension-softening behaviour after crack initiation, ECC possesses high tensile, shear and flexural strengths with strain-hardening behaviour and has exceptional crack-control capability and self-healing features, which is beneficial for improving the resilience, durability, and sustainability of concrete infrastructure [34, 35]. Thus, ECC can be carefully designed with acceptable printability for 3DCP as one of the most promising alternative to steel reinforced concrete to reduce the conventional steel reinforcement usage and enhance the durability of printed concrete structures.

In recent years, some attempts have been made to develop 3D printable ECC reinforced with polyvinyl alcohol (PVA) fibre and polyethylene (PE) fibre [28, 36-44]. Regarding PVA fibre reinforced ECC (PVA-ECC) for 3D printing, the printed ECC containing 2 vol% of 12 mm PVA fibres had tensile strength of 2.0-4.0 MPa and failure strain of 2.0-6.0% [36, 39], while the tensile strength and failure strain of the printed ECC reinforced with 2 vol% of 8 mm PVA fibres were found to be 1.0-5.5 MPa and 0.05-3.6% [37, 38, 40], respectively. Regarding 3D printing PE fibre reinforced ECC

(PE-ECC), with the incorporation of 1-1.5 vol% of 6 mm PE fibres, the tensile strength and strain capacity of printed ECC can reach 4-5 MPa and 1-3% [41], respectively. When the 12 mm PE fibres at a dosage of 1-2 vol% were added, a higher ultimate strain (3.6-11.4%) and slightly higher tensile strength (4.51-5.75 MPa) of printed ECC can be obtained [28, 42-44]. These studies indicated that the fibre length and volume fraction have a significant influence on the strain-hardening behaviour of printed ECC. Both PVA and PE fibre reinforced ECC for 3D printing were designed to be printable, buildable, and featured with strain-hardening behaviour like normal ECC. Generally, it was found that the tensile strength and ductility of printed PVA-ECC are lower than that of printed PE-ECC under the same conditions. Due to the hydrophilic property of PVA fibre, the chemical bond between the fibre without pre-treatment (such as oil coating and air-entraining agent addition) and the surrounding matrix is considerably strong, which is not preferred as it can lead to pre-mature fibre rupture before fully utilizing the maximum fibre reinforcement capability [45]. In contrast, the hydrophobicity of PE fibre increases the possibility to inadequately withstand and transfer shear stress, leading to premature debonding. This could be restrained and thus the multi-cracking behaviour can be achieved by increasing the interfacial bonding strength and compressive strength. It should be pointed out that the tensile strength of PVA fibre is relatively low (i.e., 800 - 1600 MPa), in comparison with that of PE fibres (i.e., 2500 - 3800 MPa) [46]. Compared to PVA-ECC, PE-ECC yields more robust tensile ductility with tensile strain capacity of over 4% owing to the high tensile strength, elastic modulus and hydrophobic nature of PE fibres, which is essential for the structural reliability performance. Thus, PE fibres are suitable to produce ECC with a wider compressive strength range, from 40 MPa to 120 MPa (i.e., from common to high strength), while PVA fibres are commonly used for moderate strength ECC [47, 48]. The hardened strength of the printed cementitious composites can be compromised due to the weak interfaces inevitably introduced by the layer-by-layer printing process [49]. Therefore, it is necessary to develop printable ECCs with a relatively higher strength level to compensate for the risks associated with the printing process. PE fibres are more favoured in 3D printed ECC.

Most existing studies on 3D printed ECC are mainly focused on material development (e.g., rheological control), feasibility study (e.g., printability verification), and mechanical properties of hardened specimens in comparison with normal ECC. Despite the successful development of printable ECC, there still exist many challenges. For instance, the influence of 3D printing process on microstructure and strain-hardening behaviour of printed ECC has been rarely explored. The relationship between microstructure and macroscopic hardened properties has not been investigated, which is crucial for tailoring ECC mixes for 3D printing with desired properties. Thus, further research is required to gain an in-depth understanding of the microstructure characteristics of printed ECC, especially in terms of pore structure and fibres in extruded filaments, which strongly affect the

hardened properties including mechanical properties, shrinkage, and durability.

In the actual ECC structures, the heterogeneity of raw components (e.g., inconsistent fibre diameter and fibre strength), variation in pore size and distribution and non-uniform fibre orientation and dispersion induced by 3D printing process, and variations of matrix and fibre/matrix interface properties caused by curing would lead to instability of multiple micro-cracking and tensile strain-hardening behaviour [50-52]. Unlike the traditional casting process, the extrusion-based 3DCP process may influence the microstructure characteristics of printed ECC. For fibre reinforced cementitious composites (e.g., ECC), the fibre orientation and distribution have a profound effect on the fibre bridging action and thus the toughness and mechanical behaviour. It is challenging to accurately characterise the pore structure and fibre orientation and dispersion in the printed ECC compared to normal cast ECC with the same raw materials and curing conditions. As an advanced non-destructive testing method, X-ray computed tomography (XCT) technology represents an effective approach to characterising the 3D microstructure of cementitious composites. Up to date, very limited studies are available on the XCT imaging and analysis of the 3D pore structure of printed concrete [53-55] and cast ECC [56-58]. Based on the images obtained from XCT scanning [59, 60], fluorescence [61, 62] and scanning electron microscopy (SEM) [63-66], the fibre orientation and distribution in fibre reinforced cementitious composites can be captured. For instance, digital image analysis was applied to estimate the orientation and distribution of steel fibres in the printed ultra-high performance concrete [59]. SEM images of failure section captured at backscattered electron (BSE) mode were used to detect the fibre distribution variation at micro-scale [64]. Based on the high-resolution 2D cross-sectional BSE images, it is feasible to capture and statistically analyse the fibre features in 3D printed ECC containing polymeric fibres (e.g., PE) with small diameter, high aspect ratio and highly flexible. It is of great practical significance to characterise the pore structure and fibres in extruded filament. The existing studies are mainly focused on the pore size and spatial distribution or fibre orientation only, while a systematic experimental and analytical study on the effects of microstructural characteristics including both 3D pore structure and fibre features on the tensile behaviour of 3D printed ECC is still lacking.

The main purpose of this study is to systematically investigate the relationship between tensile strain-hardening behaviour and microstructural characteristics of 3D printed PE fibre reinforced ECC. First, a series of tests were carried out to explore the effects of fabrication method (mould-cast and 3D printing), sample thickness (15 and 30 mm) and fibre length (6 and 12 mm) on the mechanical properties of PE fibre reinforced ECC including compressive strength, uniaxial tensile properties, and crack patterns. XCT and BSE imaging along with image processing and analysis was then undertaken to gain an in-depth understanding of the pore structure and fibre orientation and dispersion of normal ECC and printed ECC. Afterwards, the effects of pore structure characteristics including porosity,

pore size distribution and pore shape on the first cracking strength as well as the effects of fibre orientation and dispersion on the fibre bridge capacity were estimated to understand the underlying mechanisms of strain-hardening behaviour of printed ECC compared to normal ECC in relation to the microstructural characteristics.

2. Experimental program

2.1. Raw materials

In this study, type II 52.5 ordinary Portland cement (OPC), class I fly ash (FA), sulfoaluminate cement (SAC) based on 100% industrial solid wastes and silica fume (SF) of grade 955 as per Chinese standards [67-69] were used as binder materials, the chemical compositions and particle size distribution of which are presented in **Table 1** and **Fig. 1**, respectively. The particle size of the binders was measured by laser diffractometry (Mastersizer 2000 particle size analyzer). It is indicated that SF is the finest powder. Fine quartz sand with a maximum size of 300 μm and a mean size of 100 μm was used as fine aggregates to control the fracture toughness of ECC matrix and fibre distribution. Hydroxypropyl methyl cellulose (HPMC) with viscosity of 38000-42000 mPa·s supplied by Shanghai Chenqi Chemical Technology Co., Ltd, China was used as a viscosity modifier to avoid water drainage and increase the deformation stability or buildability of mixtures. Polycarboxylate-based superplasticizer (SP) with a water-reducing rate of 34% and a solids content of 30% supplied by Sobute New Materials Co., Ltd, China was incorporated into the mixtures to ensure the workability and thus satisfy the requirements for 3D printability.

Short-cut ultra-high molecular weight PE fibres with lengths of 6 mm and 12 mm were used to reinforce ECC matrix, the physical and mechanical properties of which are presented in **Table 2**. The typical fibre volume fraction for ECC is 2%. If the fibre content exceeds 2%, the fibres may not be uniformly distributed in the matrix and it may be difficult for ECC to be extruded out from the printing nozzle. In addition, the higher fibre content would increase the material cost. Therefore, the volume fraction of PE fibre was set as 2% for all mixtures. The morphology of raw materials (except water and admixture) is displayed in **Fig. 2**.

Table 1 Chemical compositions (wt.%) of Portland cement (OPC), fly ash (FA), sulfoaluminate cement (SAC), and silica fume (SF).

Binder	SiO_2	Fe_2O_3	Al_2O_3	CaO	MgO	SO_3	K_2O	Na_2O	LOI
OPC	20.40	3.38	4.70	64.70	0.87	1.89	0.49	0.33	3.24
FA	52.20	15.50	23.51	1.71	1.2	0.29	0.86	0.56	4.17
SAC	8.11	0.78	27.56	36.19	1.05	14.47	0.48	0.11	11.76
SF	92.90	0.08	2.49	0.84	0.99	0.36	1.64	0.28	1.04

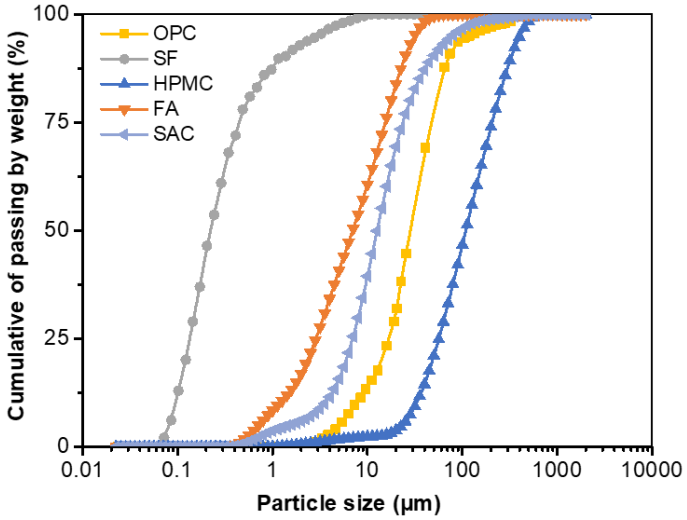

Fig. 1. Particle size distribution of OPC, FA, SAC, SF and HPMC.

Table 2 Physical and mechanical properties of PE fibre.

Fibre	Density ρ (g/cm^3)	Tensile strength f_{tf} (GPa)	Elastic modulus E_f (GPa)	Rupture elongation (%)	Length L_f (mm)	Average Diameter d_f (μm)	Aspect ratio L_f/d_f
PE	0.97	3.0	110	2.7	6/12	24	250/500

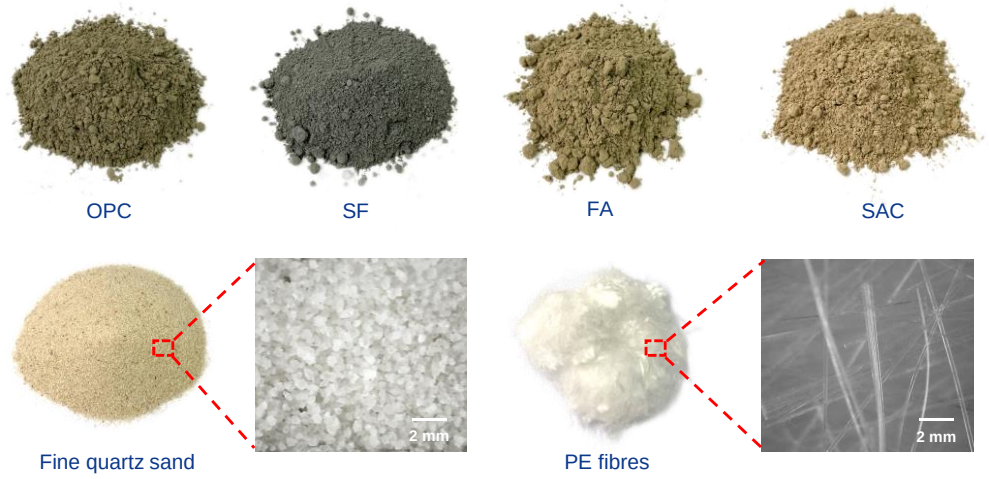

Fig. 2. Morphology of raw materials (OPC, SF, FA, SAC, fine quartz sand and PE fibres).

2.2. Mix proportions

Table 3 shows the mix proportions of ECC for normal ECC and printed ECC studied here, where "N", "L", "T" and "3DP" stand for normal, fibre length, sample thickness and printed ECC fabricated by extrusion-based 3D concrete printing, respectively. Regarding the mix ID, taking N-L6+12-T15 for example, it represents the normal ECC fabricated by mould casting, reinforced by 6 mm (1.5% by volume) and 12 mm (0.5% by volume) PE fibres, and with the thickness of specimen of 15 mm. "L6" and "L12" denote 2 vol% PE fibres with a constant length of 6 mm and 12 mm, respectively. The tensile behaviour of ECC can be affected by many factors such as fibre length, fibre dosage and matrix properties. Meanwhile, the fresh printable ECC should have excellent rheological properties

as it not only needs to be fluid enough to be pumped, but also remain stiff enough to hold the weight of subsequent deposited filaments without collapsing [70]. Higher fibre content and longer fibre length would increase the risk of fibre blockage (even clogging in the nozzle), leading to reduced mechanical properties of the printed ECC and discontinuity of extruded filaments. Reducing fibre length and dosage may be a good choice to achieve good print quality and avoid clogging for large-scale 3DCP. Thus, printable ECC with 1.5% 6 mm and 0.5% 12 mm PE fibres (i.e., 3DP-L6+12-T15) was engineered in this study to meet both printability and tensile strength and ductility as well as cost-effectiveness.

Table 3 Mix proportions of normal ECC and printed ECC (wt.%).

Mix ID	Binder				Sand	Water	SP	HPMC	PE fibre
	OPC	SAC	SF	FA					
N-L6+12-T15	0.38	0.05	0.09	0.48	0.26	0.26	0.001	0.0004	0.018 (6 and 12 mm)
N-L6+12-T30	0.38	0.05	0.09	0.48	0.26	0.26	0.001	0.0004	0.018 (6 and 12 mm)
3DP-L6+12-T15	0.38	0.05	0.09	0.48	0.26	0.26	0.001	0.0004	0.018 (6 and 12 mm)
N-L12-T15	0.38	0.05	0.09	0.48	0.26	0.26	0.001	0.0004	0.018 (12 mm)
N-L6-T15	0.38	0.05	0.09	0.48	0.26	0.26	0.001	0.0004	0.018 (6 mm)

2.3. Sample preparation

All mixtures were prepared in a 20 L planetary mixer in the laboratory environment (23 ± 1°C). **Fig. 3** shows the mixing procedure for fresh mixture of ECC. The mixture of ECC was cast into steel moulds or placed into the printer hopper after mixing. All the mould-cast specimens were de-moulded after 1 d. Then, all samples were cured in an ambient condition (23 ± 1 °C and relative humidity of 40% ± 5%) until the testing age of 28 d.

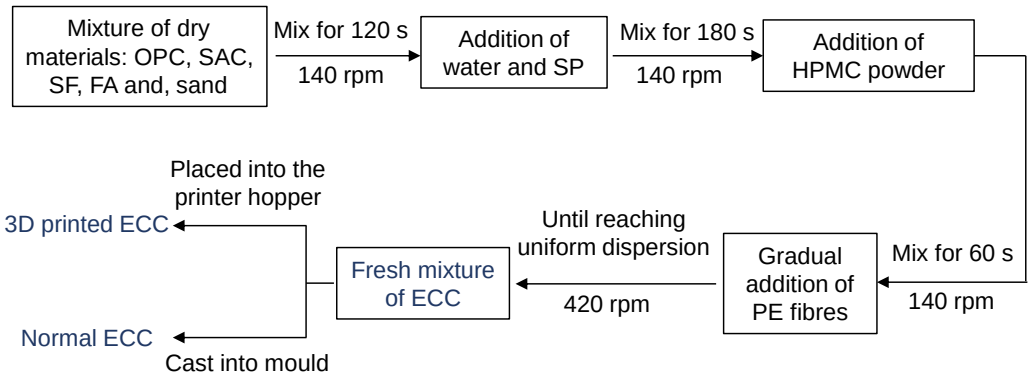

Fig. 3. Mixing procedure for ECC specimens.

The gantry-type 3D concrete printer was used to fabricate the printed specimens with dimension of 3 m × 2 m × 3 m, as illustrated in **Fig. 4a**, which consists of the combination of steel frame, drive motors, nozzle system, moving guide rail, working platform and control unit. The cone-shape extrusion device contains a compression section with a gradual groove depth mixing screw and a forming section (printer nozzle) with a rectangular opening of 30 mm × 16 mm, as shown in **Fig. 4b**. After mixing, fresh mixture of ECC was poured into the printer hopper through the batch feeding.

Then, the filament (30 mm × 15 mm) was extruded continuously from the printer head using a screw-type extruder, as displayed in **Fig. 4c**. The motion speed and extrusion speed of the printer were selected as 110 mm/s and 110 g/s, respectively.

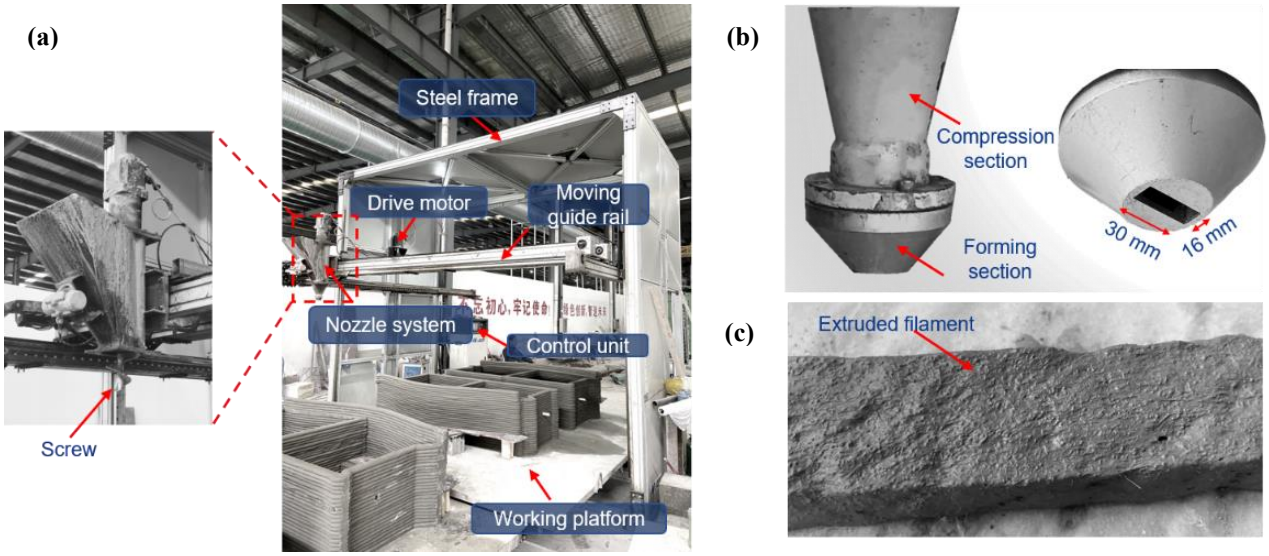

Fig. 4. (a) Gantry type extrusion-based 3D printer used in this study, (b) nozzle size, and (c) extruded filament.

2.4. *Test methods*

Table 4 presents the tests employed in this study for normal ECC and 3D printed ECC including compressive test, uniaxial tensile test, X-ray computed tomography (CT) imaging and backscattered electron (BSE) imaging, which are described in detail below. Given that N-L6+12-T15 and 3DP-L6+12-T15 have comparable tensile properties, mould-cast specimens with thickness of 30 mm were used for X-ray CT and BSE tests in comparison with 3D printed specimens, which is discussed further in Section 3.2.2.

Table 4 Testing scheme for normal ECC and 3D printed ECC of this study.

Sample	Fabrication method	Fibre volume fraction (%)		Samples for each mechanical test		Samples for each micro test	
		6 mm	12 mm	Compressive test	Uniaxial tensile test	X-ray CT test	BSE test
N-L6+12-T15	Mould-cast	75	25	3	4	-	-
N-L6+12-T30	Mould-cast	75	25	3	4	3	3
3DP-L6+12-T15	3D print	75	25	3	4	3	3
N-L12-T15	Mould-cast	0	100	3	5	-	-
N-L6-T15	Mould-cast	100	0	3	5	-	-

2.4.1. Compressive test

The compressive test was carried out to determine the 28-d compressive strength of all mixtures. The dimension of all specimens was 60 mm × 60 mm × 60 mm. The compressive test was performed on three replicated samples for each mixture using an electro-hydraulic servo testing machine with a constant displacement rate of 0.5 mm/min and the peak load values were recorded. Printed ECC

samples with the specified size were cut and grinded from a printed prism object (**Fig. 5a**) to measure the compressive strength. **Fig. 5b** shows the compressive test setup. As the main purpose of this study is to investigate the relationship between microstructure and strain-hardening behaviour of normal and printed ECC, the anisotropy of mechanical properties is not concerned and only the z-direction (printing direction) was conducted for printed samples.

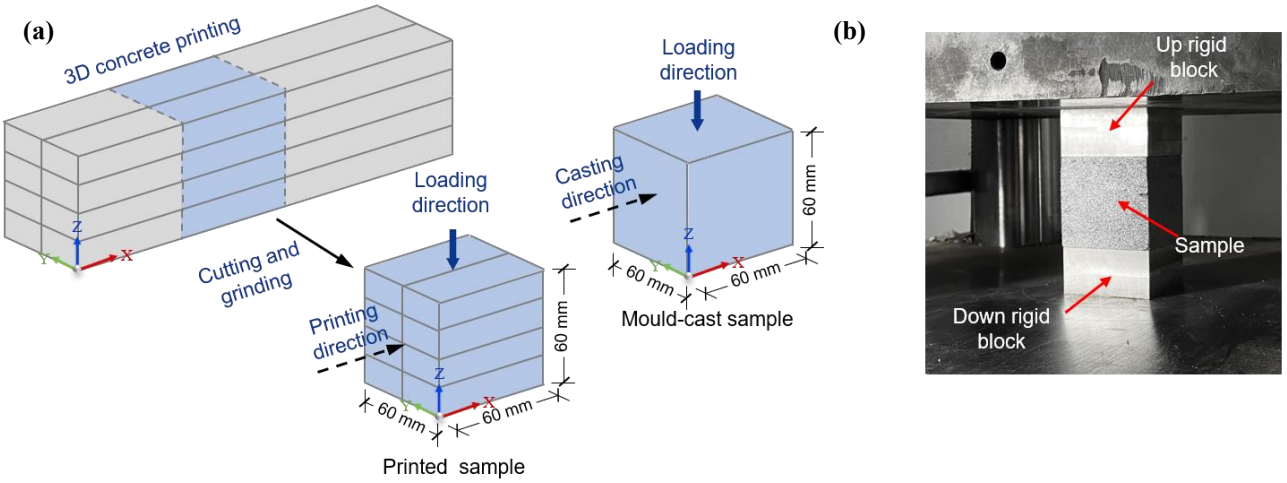

Fig. 5. Schematic diagram of compressive tests on normal and printed ECC specimens (a) casting and printing, and (b) test set up.

2.4.2. Uniaxial tensile test

Specimens with dog-bone shape were adopted to conduct the uniaxial tensile tests. The loading rate was set as 0.5 mm/min in accordance with the standards [71, 72]. The deformation in the gauge region with length of 80 mm was measured by two external linear variable displacement transducers (LVDTs). **Fig. 6** illustrates the uniaxial tensile tests on normal and printed ECC specimens. After 1 d of curing in the air, several extruded single filaments were cut into prism specimens with dimension of 330 mm × 30 mm × 15 mm, which were then placed in mould. ECC with an average 28-d compressive strength of 110 MPa was poured at both sides to form dog-bone specimens (**Fig. 6a**). After that, the printed ECC samples were cured until the testing age. The uniaxial tensile test setups for normal and printed ECC are shown in **Fig. 6b** and **c**, respectively.

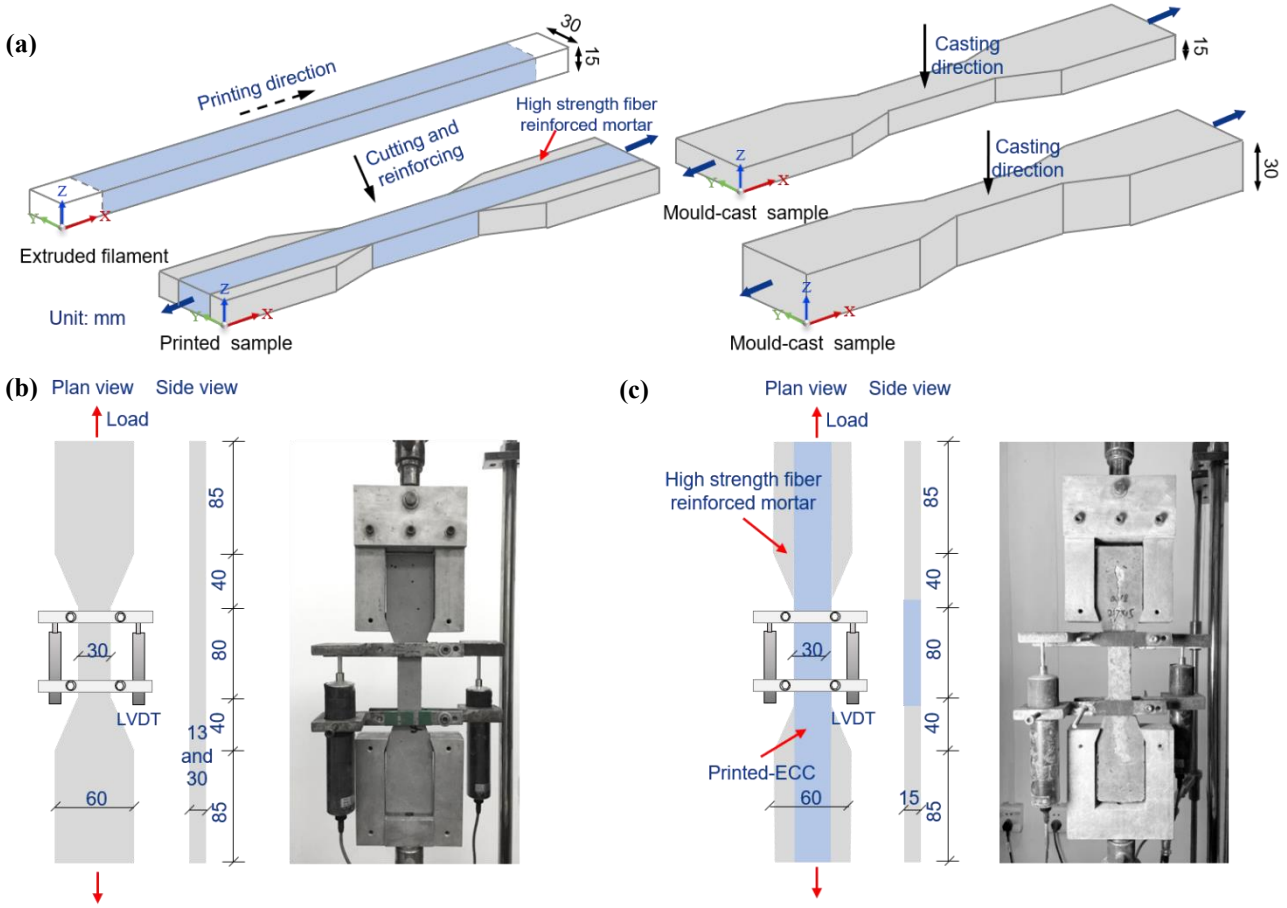

Fig. 6. Schematic diagram of uniaxial tensile tests on normal and printed ECC specimens (a) casting and printing, (b) test set up for normal ECC, and (c) test set up for printed ECC.

2.4.3. X-ray computed tomography imaging

As introduced above, the macroscopic mechanical properties of ECC are strongly dependent on the microstructure that is highly associated with the mix proportion and fabrication process (mould casting and 3D concrete printing) if the constant fibre content and length are adopted. In previous studies, HPMC was not added into the normal ECC mixtures, leading to a high content of macropores in the fresh mixtures and a certain degree of size effect [73-76]. The vibration of the cast-in-situ process and the extrusion pressure of the printer nozzle may also affect the compactness of ECC specimens. To estimate the influence of uneven microstructure, XCT imaging was conducted on the cast and printed ECC specimens (N-L6+12-T30 and 3DP-L6+12-T15) with various thickness (15 and 30 mm) after mechanical tests. A high-resolution industrial CT scanner (YXLON) was used for microstructural characterisation of both printed and cast ECC specimens, as illustrated in **Fig. 7**. The scanning parameters were set as a voltage of 195 kV and a current of 0.21 mA with a tin filter. A small piece within the gauge section of the test samples was scanned and the reconstruction was performed using Avizo software to gain images of 1024 × 1024 pixels with a 0.1 mm interval along height and a resolution of about 87.5 μm/pixel.

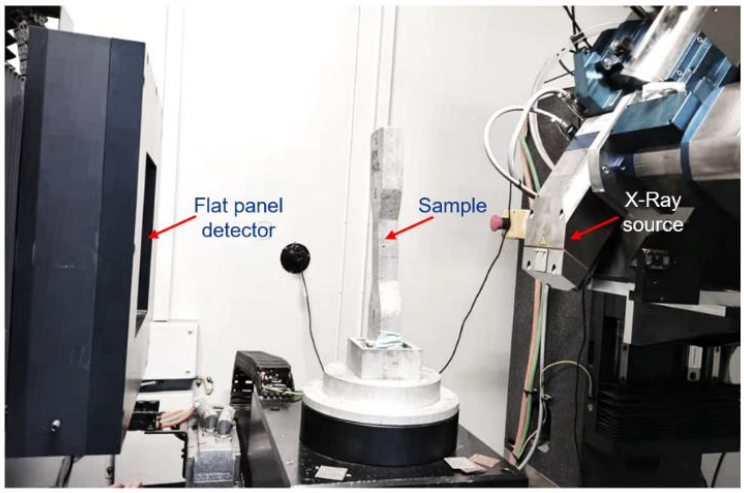

Fig. 7. Test setup for X-ray computed tomography scanning.

The size and distribution of pores in ECC along the tensile loading direction is critical for the first cracking strength of ECC which is closely related to the maximum pore area (i.e., representative pore size) perpendicular to the loading direction [56]. In this study, the image greyscale values (GSV) of the region of interest (ROI) obtained from XCT scanning were applied to characterise the pore structure of ECC using an open-source image analysis software, ImageJ. **Fig. 8** illustrates a flow chart of image processing and analysis procedure to obtain the pore structure characteristics. Small samples cut from specimens for tensile tests were used for X-ray CT scanning to obtain the high-resolution images (slices). Given the irregular dimensions of the cut samples, a series of original X-ray CT slices of the target sample with irregular area were cropped to sub-slices with regular area for 3D reconstruction and subsequent image processing and analysis. The dimensions of mould-cast samples are 28.5 mm × 15.7 mm × 14.5 mm, 27.9 mm × 15.7 mm × 14.5 mm, and 22 mm × 11.4 mm × 11.0 mm, respectively, while that of printed samples are 20.2 mm × 13.3 mm × 14.8 mm, 20.4 mm × 12.3 mm × 14.8 mm, and 21.3 mm × 11.2 mm × 14.8 mm, respectively. Due to different physical density, the pore and solid phases in hardened ECC samples exhibit an obvious difference in grey level, as seen in the sub-slice image in Fig. 8a. Based on the grey-level histogram, the global thresholding method was employed for image segmentation and a constant threshold value of 45 (grey level) was determined to distinguish pore from solid phases. More details about the global thresholding method can be found in Ref. [77]. In this study, the largest pore with the maximum area in each slice of image was selected to determine the pore size in 2D. To facilitate the calculations, the pores are assumed to be in ellipse. Afterwards, the pore structure characteristics of cast and printed ECC in terms of pore size distribution (including the maximum and minimum pore sizes of D_{max} and D_{min}) and porosity (P_{2D} in 2D and P_{3D} in 3D) can be obtained as follows:

$$P_{2D} = \frac{N_{pore}}{N_{image}} \tag{1}$$

$$D_{max} = l_{AB} \tag{2}$$

$$D_{min} = \frac{S_{equal}}{\pi \cdot D_{max}} \tag{3}$$

$$P_{3D} = \frac{V_{pore}}{V_{total}} \tag{4}$$

where N_{pore} is the pixel number of pores in each image, N_{image} is the total pixel number in each image, l_{AB} is the longest distance between two points at the pore edge (mm), i.e., the long axis of the equivalent ellipse, S_{equal} is the equivalent ellipse area of the largest pore in each image, D_{max} and D_{min} denote the lengths of long axis and short axis of the equivalent ellipse (mm), respectively, V_{pore} is the total pore volume of ROI, and V_{total} is the total volume of ROI.

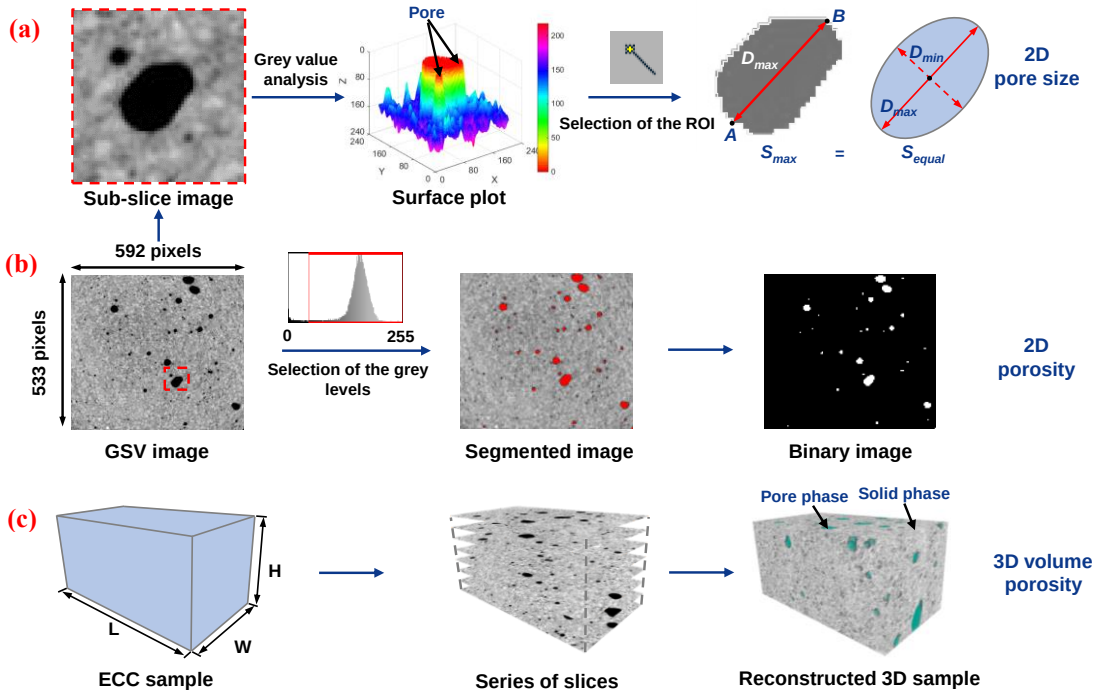

Fig. 8. Flow chart of image processing to determine (a) 2D pore size, (b) 2D porosity, and (c) 3D volume porosity.

2.4.4. Backscatter electron imaging

In addition to pore structure, the non-uniform distribution and orientation of fibres in ECC are also crucial for mechanical properties of ECC through fibre-bridging effect. To determine the fibre distribution and orientation in normal cast ECC and printed ECC, the analysis of BSE images was carried out. The samples taken from the gauge region of each dog-bone shaped specimen after uniaxial tensile tests were polished and prepared for BSE imaging, as demonstrated in **Fig. 9**. More details about the sample preparation for BSE imaging can be found in Ref. [78].

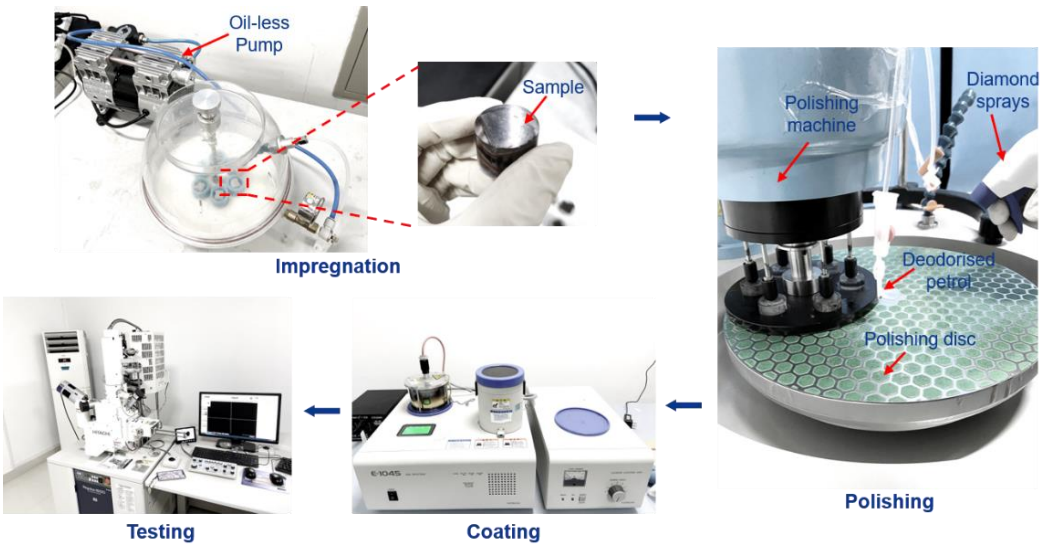

Fig. 9. Sample preparation for backscatter electron (BSE) imaging.

To capture the fibre dispersion, the images with 20000 μm × 11000 μm of the saw-cut samples were divided into 15 × 4 units, as per a pervious study [66]. Each unit contains a size of 1269.8 μm × 952.4 μm. Regarding fibre orientation, the cross-section of fibres on the cut surface can form three patterns (circle, ellipse, and strip) when the specimen is cut perpendicular to the direction of tension, as illustrated in **Fig. 10a**. Here, the fibre inclination angle θ is defined as the angle between the fibre axis and the normal direction of the fracture surface, which can be calculated using Eq. (5). **Fig. 10b** displays the image processing and analysis procedure to detect the fibre orientation, where a two-parameter function was used to describe the probability density function $p(\theta)$ as Eq. (6) [79], and thus the cumulative distribution function $P(\theta)$ of the fibre orientation can be calculated by Eq. (7). After that, the actual cumulative distribution function can be obtained by fitting Eq. (7).

$$\theta = arccos\frac{d_f}{l_f} \tag{5}$$

$$p(\theta) = \frac{(sin\theta)^{2r-1}(cos\theta)^{2q-1}}{\int_{\theta_{min}}^{\theta_{max}}(sin\theta)^{2r-1}(cos\theta)^{2q-1}d\theta} \tag{6}$$

$$P(\theta) = \int_0^{\theta} p(\theta)d\theta \quad 0 \le \theta \le \pi/2 \tag{7}$$

where d_f is the actual fibre diameter defined as the minor axis length per dispersed fibre, l_f is the major axis length per dispersed fibre, r ($\geq 1/2$) and q ($> 1/2$) are the shape parameters [80], and θ_{min} (0) and θ_{max} ($\pi/2$) are the theoretical minimum and maximum inclination angles of fibres.

As the crack bridging stress at a given crack opening is proportional to the fibre volume fraction, a high uniformity of fibre dispersion in the cross-section would result in a robust tensile strain capacity of ECC. The local fibre volume fraction V_l (%) can be used to quantify the variation of fibre volume fraction as follows:

$$V_l = \frac{N_f \times S_f}{S_a} \tag{8}$$

where N_f is the number of fibres per image, S_f is the total fibre area per image (μm^2), and S_a is the physical size (1269.8 μm × 952.4 μm) for each BSE image at a magnification of 150×.

Furthermore, the fibre distribution coefficient α_f denoting the number of fibres per unit area was adopted to quantitatively evaluate the fibre dispersion degree in hardened ECC, as described in Eq. (9) [81, 82]. The closer the value of α_f is to 1, the more uniform the fibre dispersion is in the picked area.

$$\alpha_f = exp\left[-\frac{1}{\bar{x}}\sqrt{\frac{\sum(x_i-\bar{x})^2}{n}}\right] \quad (9)$$

where $\bar{x}$ represents the average number of fibres in all images, x_i denotes the number of fibres in the i-th image, and n is the total number of all images.

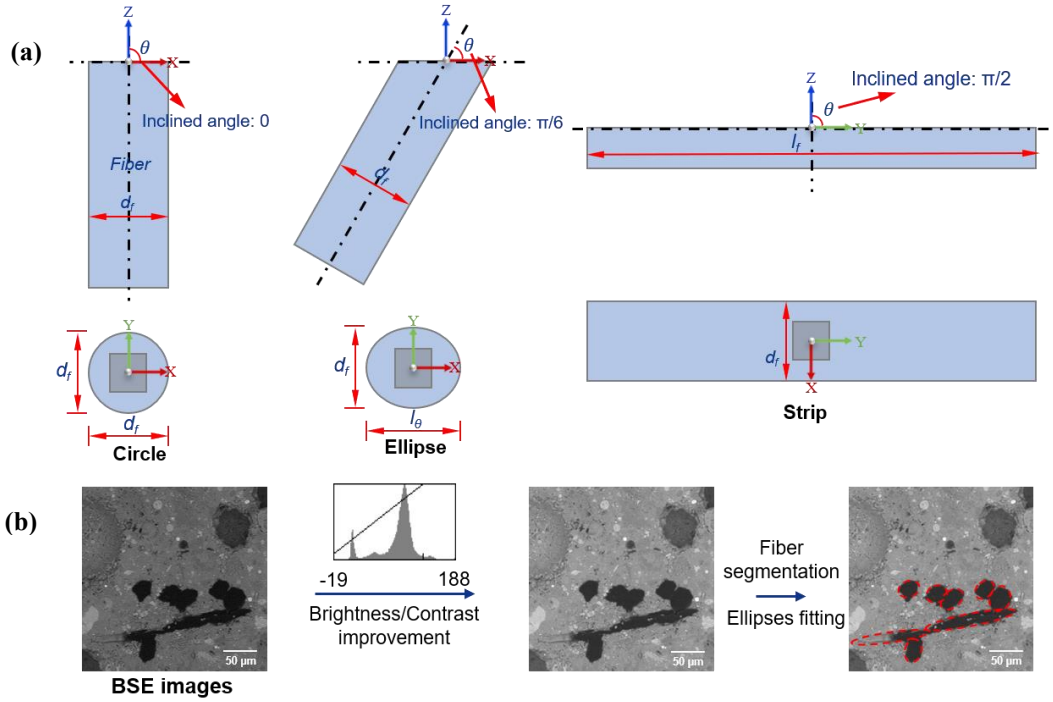

Fig. 10. (a) Schematic image of inclination angle of fibre; (b) Image processing and analysis procedure to evaluate the fibre orientation in ECC.

3. Results and discussion

3.1. Compressive strength

Fig. 11 presents a comparison of the 28-d compressive strength of all ECC specimens produced by mould casting and 3D printing, reinforced with 6 mm and 12 mm PE fibres. As only the mixtures N-L6+12-T15 and N-L6+12-T30 have the thickness difference, the compressive strength of N-L6+12-T15 is selected for comparison. As seen in **Fig. 11**, the mixture N-L6-T15 exhibited the highest compressive strength (i.e., 61.03 MPa) among all mixtures containing 6 mm fibres, which was 24.1% and 24.8% respectively higher than that of N-L6+12-T15 and N-L12-T15. According to previous studies [83-86], the addition of fibres can simultaneously bring both positive and negative effects on

the compressive strength of cementitious composites, which can be associated with the physical and mechanical properties of fibres, especially length and stiffness. The reduction in compressive strength with the incorporation of PE fibres can be mainly attributed to the less compactness of the composite and the longer fibres (12 mm) would have a greater weakening effect on the compressive strength of ECC specimen at a given fibre content.

Regarding the influence of production methods, the compressive strength of 3DP-L6+12-T15 was 4% higher than that of N-L6+12-T15 when the load was applied along z-direction, which is consistent with that presented in Ref. [44]. It can be explained by the fact that (1) the screw's continuous extrusion pressure eliminates part of large pores induced by the addition of HPMC, resulting in a more compact microstructure and more pores with uniform sizes in the extruded filament; (2) the rectangle of the print nozzle makes larger contact area between adjacent filaments. It is worth noting that the drop in compressive strength for the mould cast ECC specimens was not significant when the loading direction was perpendicular to the layer interface, suggesting that the interface of rectangular filament had no obvious influence on the compressive strength of ECC with mould casting. The compressive strength of printed ECC varied due to the number of interfaces and mechanical properties of the interface and thus it is worth to explore the anisotropy of compressive properties of printed specimens with different interface numbers and interfacial pore characteristics [87]. Besides, compared to mould cast ECC specimens, the printed ECC specimens exhibited a relatively greater variation in compressive strength, which can be ascribed to the presence of some weak interfaces between printed layers.

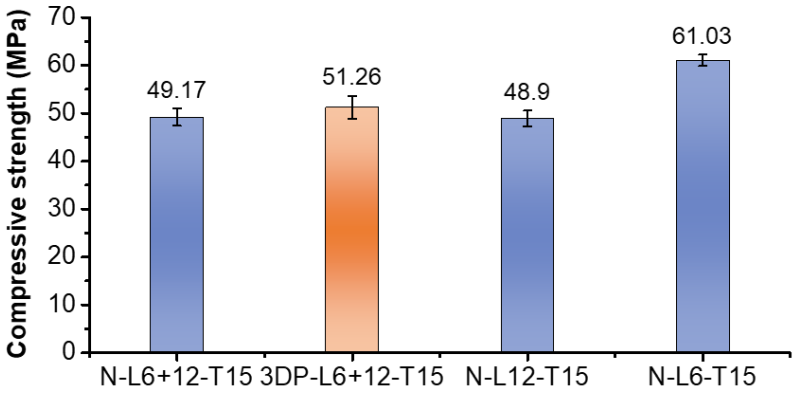

Fig. 11. Compressive strength of ECC specimens at 28 d.

3.2. Uniaxial tensile behaviour

3.2.1. Tensile stress-strain response and failure patterns

Fig. 12 shows the uniaxial tensile stress-strain curves of all ECC mixtures at 28 d, indicating that all mixtures exhibited tensile strain-hardening behaviour and high ductility along with clear multiple micro-cracking (**Fig. 13**). It should be mentioned that the tensile stress-strain curve with ductility close to the average one of different curves for each mixture was selected as the typic curve for

comparison between different mixtures, as shown Fig. 12f. Typically, the tensile stress-strain curve of PE fibre reinforced ECC consists of three distinct regions including a linear elastic region, a strain-hardening region, and a strain-softening region [88]. The tensile stress corresponding to the transition point of the linear elastic and strain-hardening regions is regarded as the first cracking strength (σ_{tc}), while the tensile stress and strain at the transition point of the strain-hardening and strain-softening regions are defined as the direct tensile strength or ultimate tensile strength (σ_{tu}) and ultimate tensile strain capacity (ε_{tu}). As seen in **Fig. 12**, no obvious difference can be observed for the first cracking strength of all ECC specimens. Among all mixtures, N-L12-T15 containing 12 mm PE fibres showed the most significant strain-hardening behaviour, while the strain-hardening region of N-L6-H15 with 6 mm PE fibres was relatively short. Based on the tensile stress-strain curves and recorded failure patterns, the typical tensile properties and cracking details of mould cast and printed ECC can be obtained, which are presented and discussed in detail below.

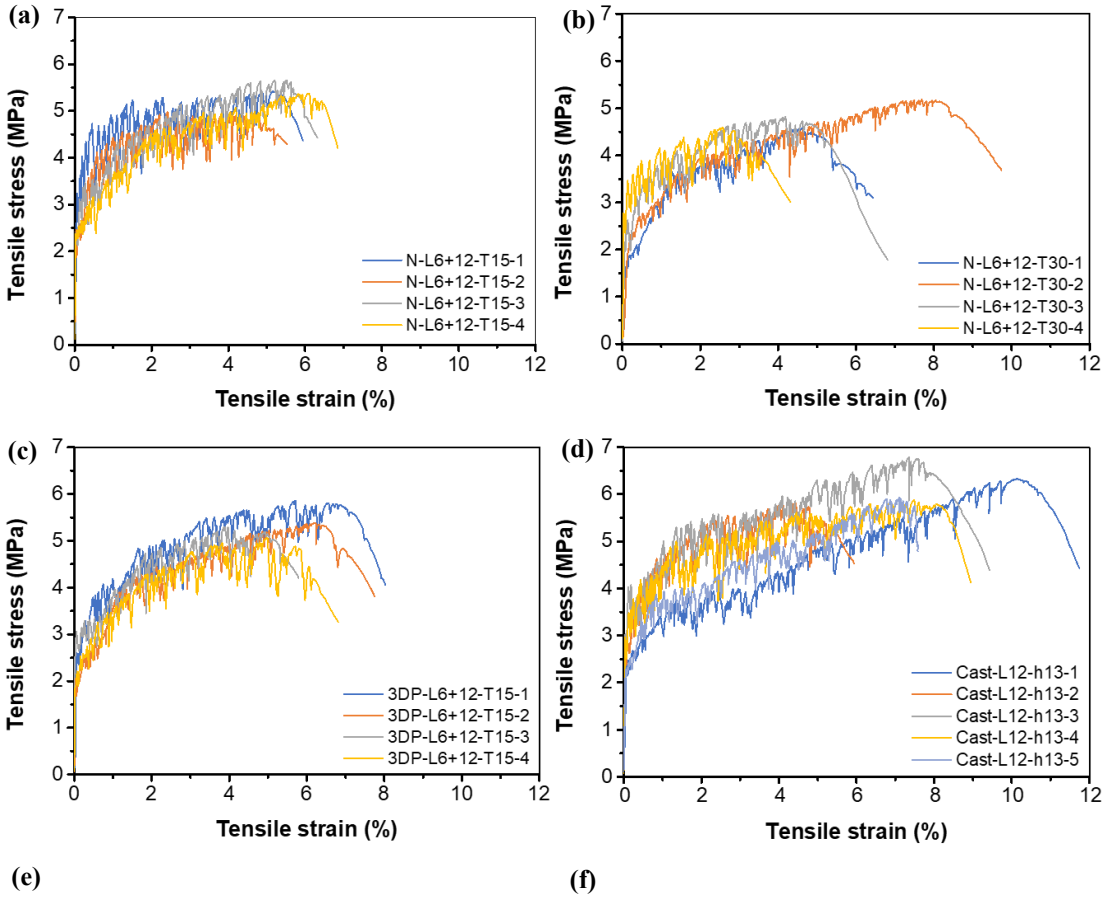

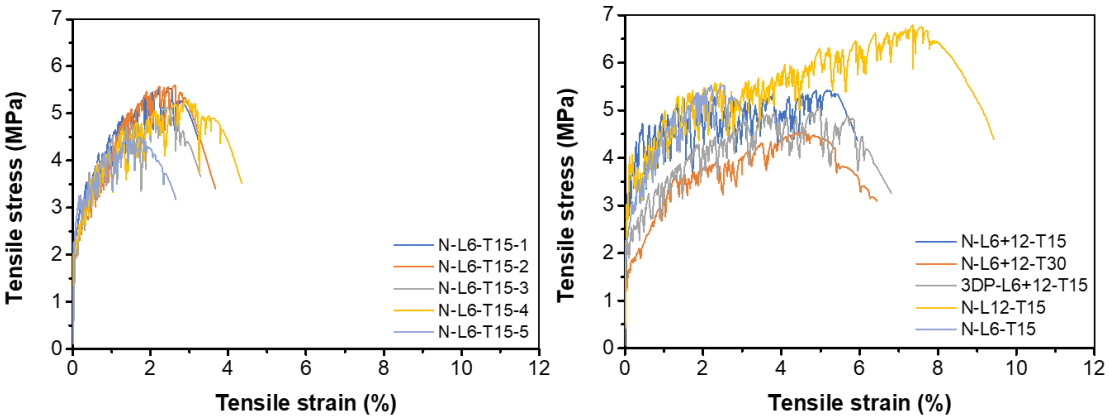

Fig. 12. Tensile stress-strain curves of (a) N-L6+12-T15, (b) N-L6+12-T30, (c) 3DP-L6+12-T15, (d) N-L12-T15, (e) N-L6-T15, and (f) typical curves for different mixtures.

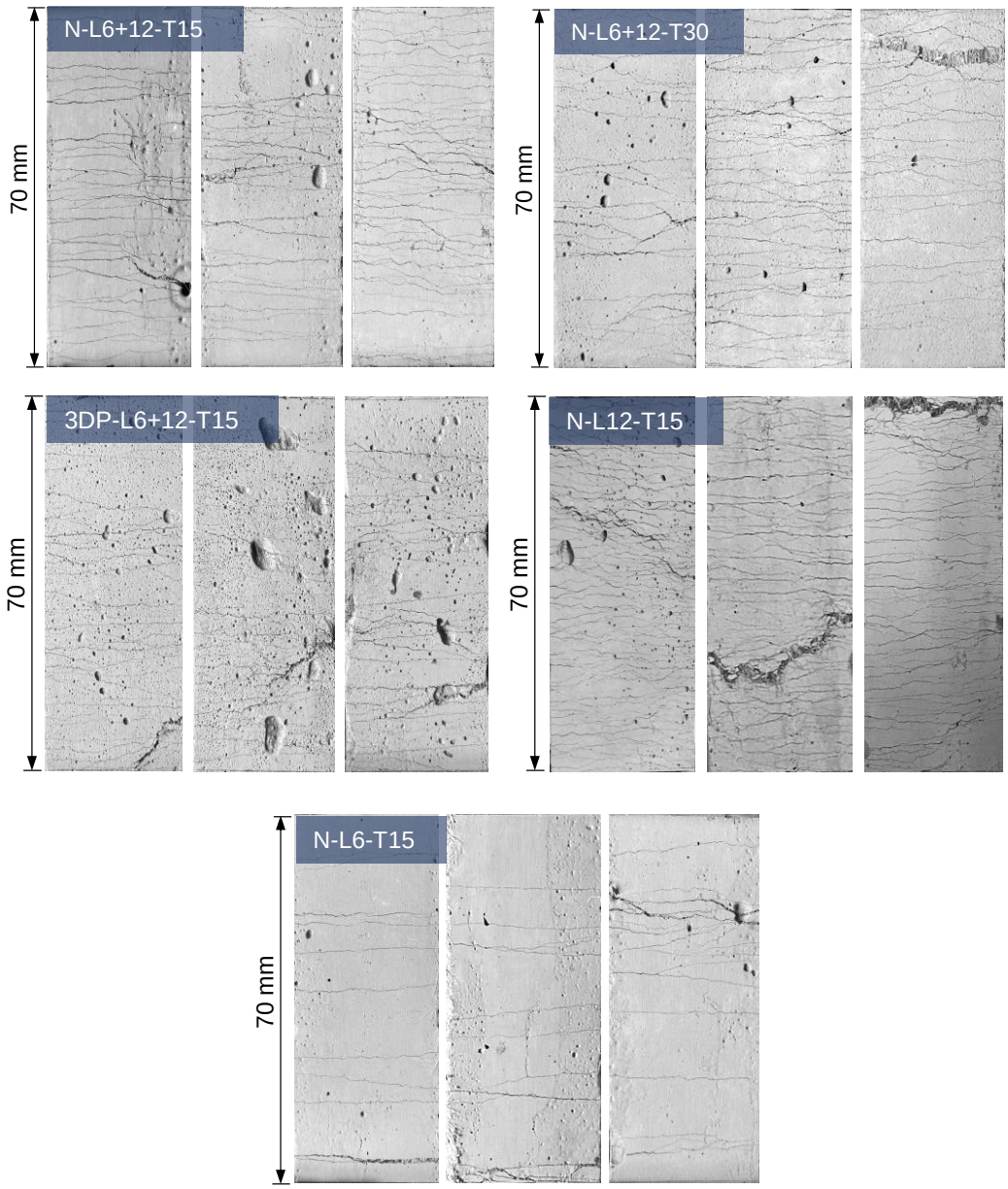

Fig. 13. Typical tensile cracking patterns of all ECC mixtures.

3.2.2. Tensile properties

Table 5 summarises the tensile properties and cracking details of ECC, including first cracking strength (σ_{tc}), ultimate tensile strength (σ_{tu}), ultimate tensile train capacity (ε_{tu}), number of cracks (N_c), and the average crack width (w_c). Regarding the ECC specimens containing 6 mm and 12 mm PE fibres, the first cracking strength was increased slightly with the increase of 12 mm fibre dosage, which is in good agreement with the findings reported in a previous study [88]. The average tensile strain capacity went up significantly with the increasing content of 12 mm fibre. With the increase of 12 mm fibre content portion from 25% to 100%, the tensile strain capacity of ECC was increased by 113% and 198%, respectively, which can be mainly ascribed to the fibre bridging effect. As per the micromechanical bridging theory, the fibre bridging action increases with the increase of fibre length in a certain range, while 2.0 vol% 6 mm fibres with a maximum embedment length of only 3 mm are too weak to retain the steady crack propagation [89, 90]. The ultimate tensile strength followed a similar changing trend, which was slightly increased from 5.20 MPa (N-L6-T15) to 6.15 MPa (N-L12-H15), which is consistent with that presented in Ref. [91].

As seen in **Table 5**, no obvious difference can be observed for the 28-d first cracking strength of ECC specimens with different thickness, i.e., N-L6+12-T15 and N-L6+12-T30. Specifically, as the thickness of ECC specimen was increased from 15 mm to 30 mm, σ_{tu} and ε_{tu} declined from 5.36 MPa to 4.79 MPa and from 5.22% to 4.77%, respectively. The specimen N-L6+12-T30 experienced the highest variation in tensile strain capacity (**Fig. 12b**). The tensile properties of ECC may be strongly associated with the mechanical properties of matrix, the pore distribution and the fibre/matrix interface features. Thus, the decrease and variation in tensile ductility for thicker ECC specimens (N-L6+12-T30) may be ascribed to the poor fibre dispersion (i.e., poor fibre bridging efficiency) and more initial air voids (i.e., reduced fracture toughness) in the matrix.

In addition, the test results indicated that the fabrication method (i.e., mould casting or 3D concrete printing process) has little effect on the first cracking strength, ultimate tensile strength, and tensile strain capacity of ECC, implying that the mould cast plane ECC specimens (N-L6+12-T15) and 3D printed ECC specimens (3DP-L6+12-T15) with the same low thickness of 15 mm had similar tensile properties. The ultimate tensile strength and tensile strain capacity of 3DP-L6+12-T15 (15 mm) were found to be 12.7% and 9.4% respectively higher than that of N-L6+12-T30 (30 mm), suggesting that more robust composite ductility can be achieved by the extrusion-based 3D printing process for ECC with appropriate thickness. For dogbone-shaped plane ECC specimens, the larger transverse cross-section of the block specimen allows the relatively uniform 3D distribution of fibres and resembles that in a real structure [34]. Therefore, the block specimens for mould casting can be used to compare the tensile properties of cast-in-situ specimens and printed specimens.

Table 5 Tensile properties of all ECC specimens.

Sample	σ_{tc} (MPa)	σ_{tu} (MPa)	ε_{tu} (%)	N_c	w_c (μm)

N-L6+12-T15	2.47±0.35	5.36±0.25	5.22±0.74	61±6	73.88±1.17
N-L6+12-T30	2.21±0.41	4.79±0.25	4.77±1.85	46±9	96.08±10.27
3DP-L6+12-T15	2.40±0.39	5.40±0.29	5.22±0.84	70±6	73.47±13.00
N-L12-T15	2.63±0.28	6.15±0.36	7.31±1.83	94±29	68.69±12.84
N-L6-T15	2.27±0.16	5.20±0.39	2.45±0.42	21±4	110.92±14.42

3.2.3. Multiple micro-cracking

In **Table 5**, N_c represents the average number of cracks in 80 mm gauge length, and w_c denotes the ratio of the elongation to the number of cracks (μm), i.e., $w_c = 80000 \times \frac{\varepsilon_{tl}}{N_c}$, where ε_{tl} denotes the tensile strain at the last plunge of stress-strain curve. The cracking patterns of different ECCs after load removal shown in **Fig. 12** were consistent with the obtained tensile stress-strain curves along with strain-hardening and significant multiple cracking features for all mixtures. Overall, the average crack width reduced remarkably with the increase of average number of cracks. Most saturated distributed micro-cracks can be found across the entire section of the specimen N-L12-T15, followed by 3DP-L6+12-T15, N-L6+12-T15, N-L6+12-T30, and N-L6-T15, leading to the highest tensile strain capacity of N-L12-H15. For instance, the average residual crack widths of N-L6+12-T15, 3DP-L6+12-T15 and N-L12-T15 were in the range of 68.69-73.88 μm, similar to those reported for the typical PE fibre-reinforced ECC [58, 92, 93]. The fine crack widths (typically below 100 μm) can be beneficial for long-term durability and self-healing performance of cast and 3D printed PE-ECC developed in this study [34, 94]. The average crack widths of N-L6+12-T30 and N-L6-T15 were relatively larger, which were close to 100 μm and over 100 μm, respectively due to the relatively poor fibre bridging capacity induced by the short fibre length, random pore size distribution and random fibre dispersion. The effects of pore and fibre distribution will be further verified with the XCT and BSE results presented in the following sections. In general, a suitable ECC must achieve tensile strain capacity of over 4% with saturated multiple cracks and 28-d compressive strength of around 51.26 MPa for structural application [95, 96]. The results indicated that the 3D printed plane ECC containing 1.5% 6 mm and 0.5% 12 mm PE fibres by extrusion-based 3D printing can well meet this criterion as it had a unique tensile strain capacity of over 5%, autogenous crack width control (less than 100 μm), and compressive strength of over 50 MPa.

3.3. Pore structure characteristics

3.3.1 Pore size distribution and porosity

Fig. 14 illustrates the 3D pore structures of the specimens extracted from normal ECC and printed ECC, along with the equivalent ellipse centre coordinates of the pore with the largest area in each slice. Overall, the cast ECC specimens had more large pores per unit volume compared to the printed

ECC specimens. Natural pores with irregular ellipsoid shape were randomly distributed in the matrix of the two and some small pores were attached to the surface of larger pores. Aside from the visual observation, other important information including the volume and size of each pore can be obtained. The frequency histograms of pore volume for normal ECC and 3D printed ECC are presented in **Fig. 15** to quantify the pore size distribution. It should be noted that the pore volume data of three samples for each fabrication method was combined for analysis. As seen in **Fig. 15**, the pore volume in the matrix was mainly within 1 mm^3 for both fabrication methods. In detail, the pores with size ranging from 0 to 0.1 mm^3 in normal ECC and printed ECC accounted for 95.3% and 97.3% of the total pore volume, respectively. Besides, for ECC with volume of 10000 mm^3, the number of pores larger than 1 mm^3 in the normal specimen was greater than that in the printed specimen. The number was, on equivalent, measured as 12.5 per 10000 mm^3 for the printed ECC and 31.3 per 10000 mm^3 for the normal ECC. Herein, according to the pore size classification given in Refs. [53, 97, 98], the pores in the reconstructed XCT images can be divided into three groups based on pore diameter, i.e., small pore: < 0.01 mm^3, medium pore: 0.01-1 mm^3, and large pore: ≥ 1 mm^3.

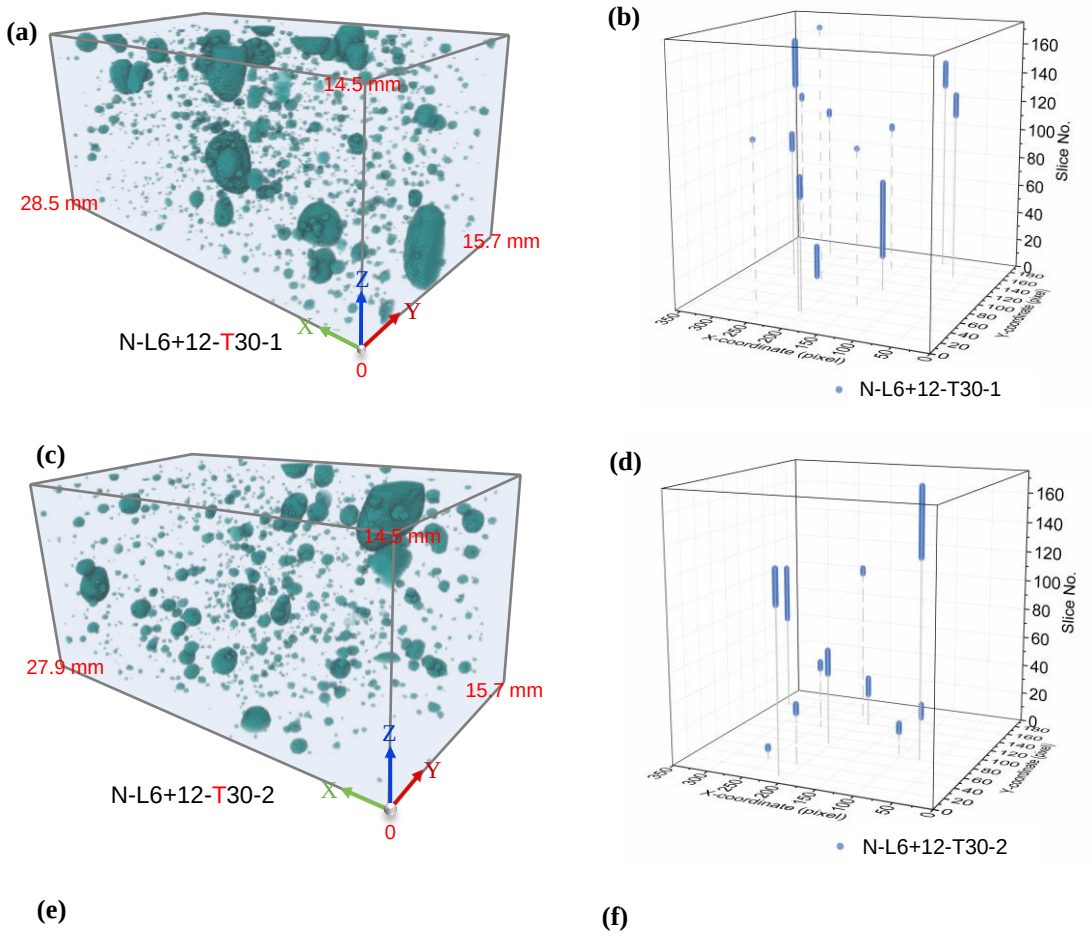

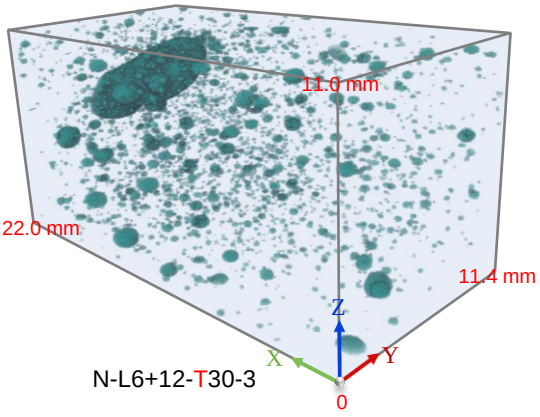
11.0 mm
22.0 mm
11.4 mm
Z
X
Y
0
N-L6+12-T30-3

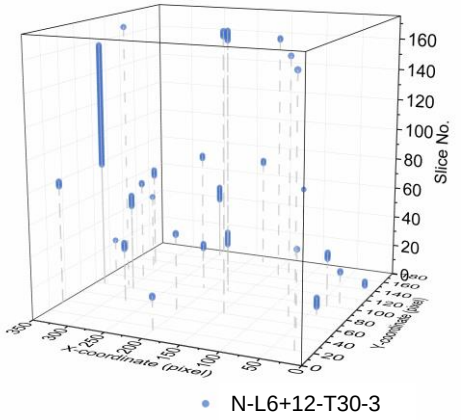
Slice No.
X-coordinate (pixel)
Y-coordinate (pixel)
N-L6+12-T30-3

(g)

(h)

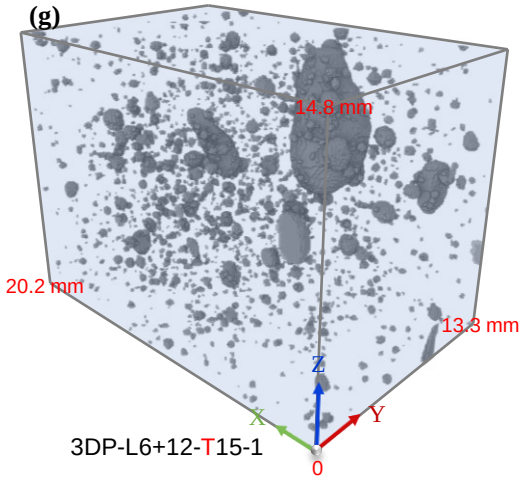
14.8 mm
20.2 mm
13.3 mm
Z
X
Y
0
3DP-L6+12-T15-1

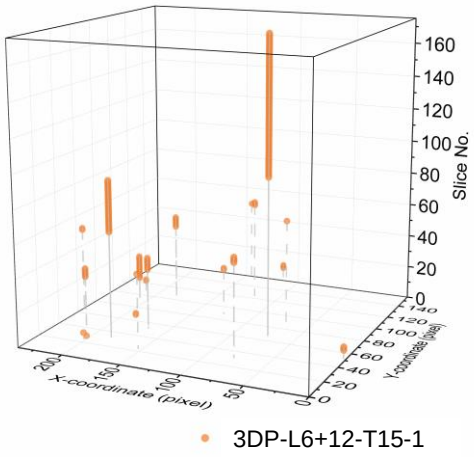
Slice No.
X-coordinate (pixel)
Y-coordinate (pixel)
3DP-L6+12-T15-1

(i)

(j)

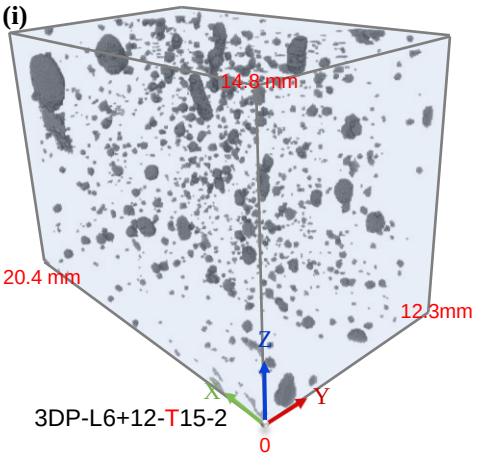
14.9 mm
20.4 mm
12.3mm
Z
X
Y
0
3DP-L6+12-T15-2

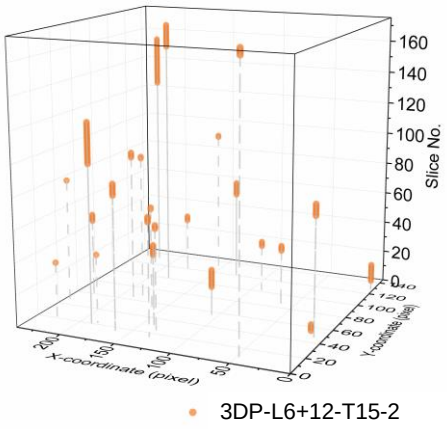
Slice No.
X-coordinate (pixel)
Y-coordinate (pixel)
3DP-L6+12-T15-2

(k)

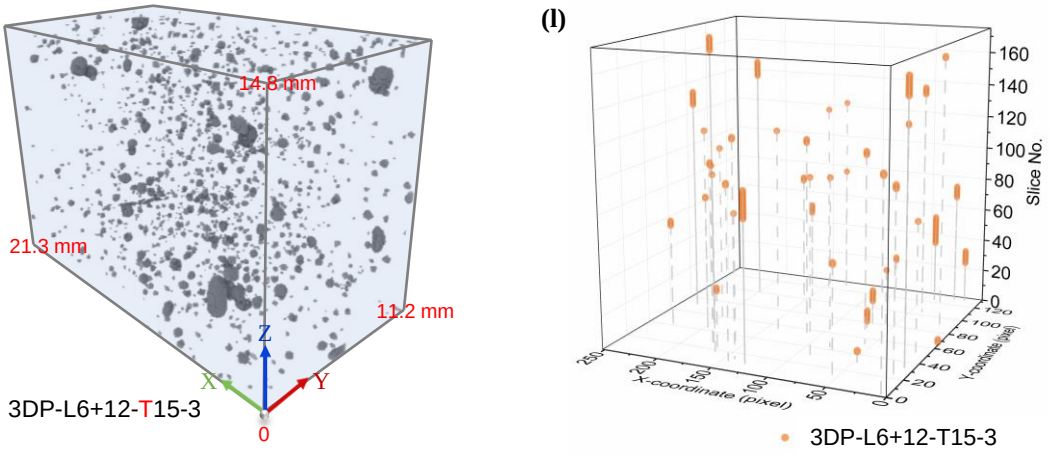

Fig. 14. 3D pore structures of the samples extracted from the normal and the printed ECC, and the equivalent ellipse centre coordinates of the pore with the largest area in each slice.

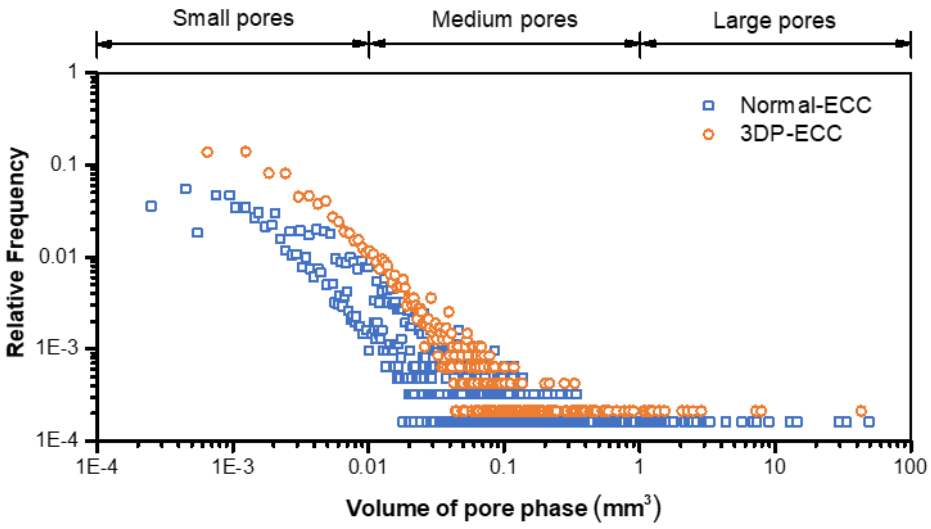

Fig. 15. Pore volume frequency histograms for normal ECC and 3D printed ECC.

As the largest pores play a more crucial role in determining the cracking strength of ECC, more emphasis should be placed on the extreme value of a single pore area in the specimen perpendicular to the stress direction. Based on XCT images, the 2D pore diameter and porosity and 3D porosity of normal ECC and printed ECC were obtained and displayed in **Fig. 16**. Given that block samples can provide more real microstructural characteristics, it is also reasonable here to use conventionally mould cast ECC specimens with thickness of 30 mm (i.e., N-L6+12-T30) as counterparts for comparison of porosity. As seen in **Fig. 16a** and **b**, D_{max} and D_{min} followed the same change trend, where D_{max} fluctuated greatly while D_{min} varied slightly. Moreover, normal ECC varied in the range of 0.08-0.81 mm, which is slightly greater than that for printed ECC, i.e., 0.05-0.68 mm. The printed samples had maximum long axis distances of 4.27, 2.47, and 1.50 mm, respectively, which was smaller than that for normal specimens, i.e., 7.13, 5.31, and 4.97 mm, respectively. Correspondingly, the single maximum pore area in 2D transverse cross-section for the normal ECC was 1.9 (15.96/8.56) times larger than that of the printed ECC, indicating that the macropore size in the normal specimen

was larger than that of the printed specimen. More specifically, the difference between them was not significant, as confirmed by the pore volume data, which showed that the maximum pore volume of the normal ECC specimen (49.25 mm^3) was 1.15 times larger than that of the printed ECC specimen (42.91 mm^3).

Based on the analysis of 2D images, the porosity also showed a positive correlation with D_{max}. As seen in **Fig. 16c**, the maximum porosity of the normal ECC specimen (7.99%) was 1.74 times that of the printed ECC specimen (4.58%). Additionally, the total average porosity of normal and printed ECC was found to be 2.5% and 1.2%, respectively, which is consistent with that reported in Refs. [99, 101] that the printed concrete possesses a lower porosity compared to mould casting concrete. In terms of overall porosity in 3D, normal ECC specimens had an average porosity of 2.52% that is higher than that of the printed ECC specimens, i.e., 1.26%, but both specimens exhibited a large variation, as depicted in **Fig. 16d**. This can be explained by the fact that (1) the screw extrusion pressure of the printer may reduce the size of large pores in the printed ECC; (2) the higher viscosity of the fresh material induced by the addition of thickening agents and mechanical vibrations of the mould casting method makes the larger pores isolated. Thus, it can be concluded that the printed ECC had a smaller probability of large pores compared to the normal ECC matrix, leading to a less variation in the tensile properties, as presented in **Table 5** and discussed in detail in Section 3.2.

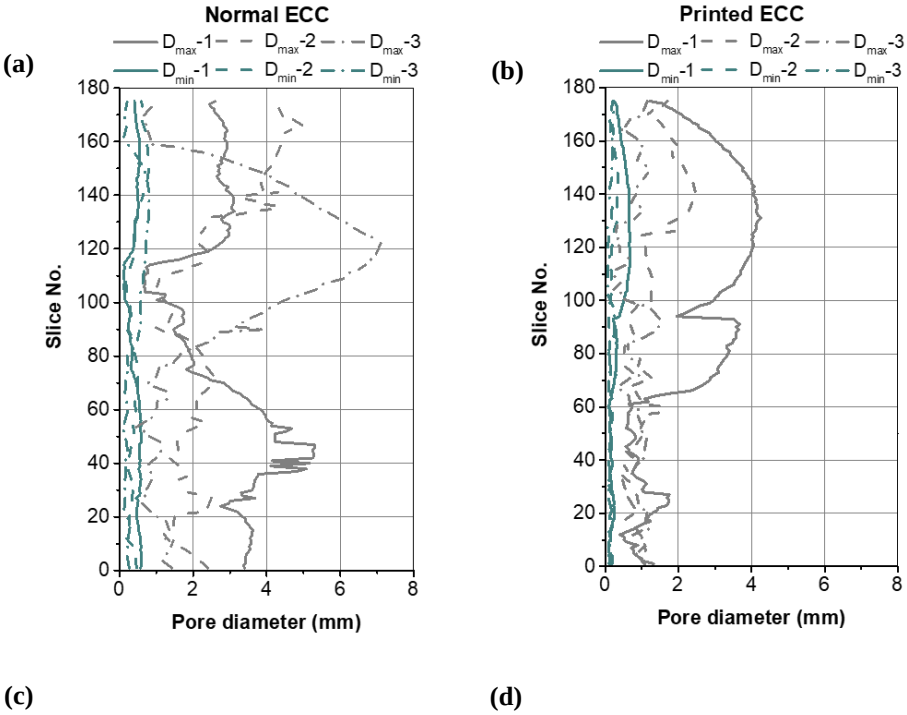

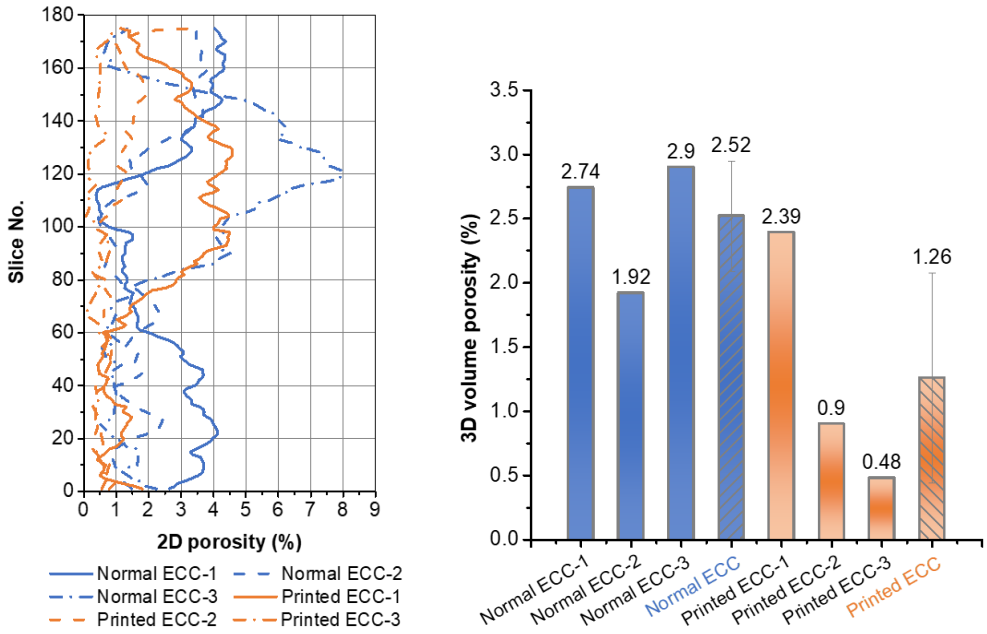

Fig. 16. Maximum and minimum pore sizes (D_{max} and D_{min}) of (a) normal ECC and (b) printed ECC, and (c) porosity in 2D and (d) porosity in 3D of normal ECC and printed ECC.

3.3.2 Pore shape

Apart from the pore size distribution and porosity, the pore shape, particularly the shape of large pores should also be considered when evaluating tensile behaviour of ECC. As illustrated in the 3D XCT images in Section 3.3.1, the shape of small and medium pores in ECC looked relatively spherical, while the shape of large pores varied considerably, which agrees well with that found in Ref. [53]. In this study, the focus is placed on the shape difference of large pores with volume over 1 mm^3. **Fig. 17a** displays the representative shape of large pores in normal ECC and printed ECC with arrows indicating the direction of tensile loading. The large pores in both normal ECC and printed ECC specimens had a similar shape, ranging from near spherical to elongated ellipsoidal. Thus, the stress concentration around the pores in these two specimens were comparable in the cross sections perpendicular to the direction of force. **Fig. 17b** illustrates the ratio (the long axis to the short axis) of the equivalent area of the largest pore in each slice of normal ECC and printed ECC, which is used to evaluate the pore morphology. The ratio close to 1 means that the pores on the slice are shaped like a circle. In general, the normal and printed ECC specimens indicated a similar aspect ratio of pores, with a variation in the range of 5-10. The average aspect ratios of pore in normal ECC specimens were 6.52%, 5.72%, and 6.33%, respectively, compared to that of 7.01%, 6.62%, and 5.73% in printed ECC specimens. In summary, the pore morphology in a single printed filament was nearly identical to that of normal ECC, which can be ascribed to the existence of a single extruded filament of printed ECC for analysis without the interface.

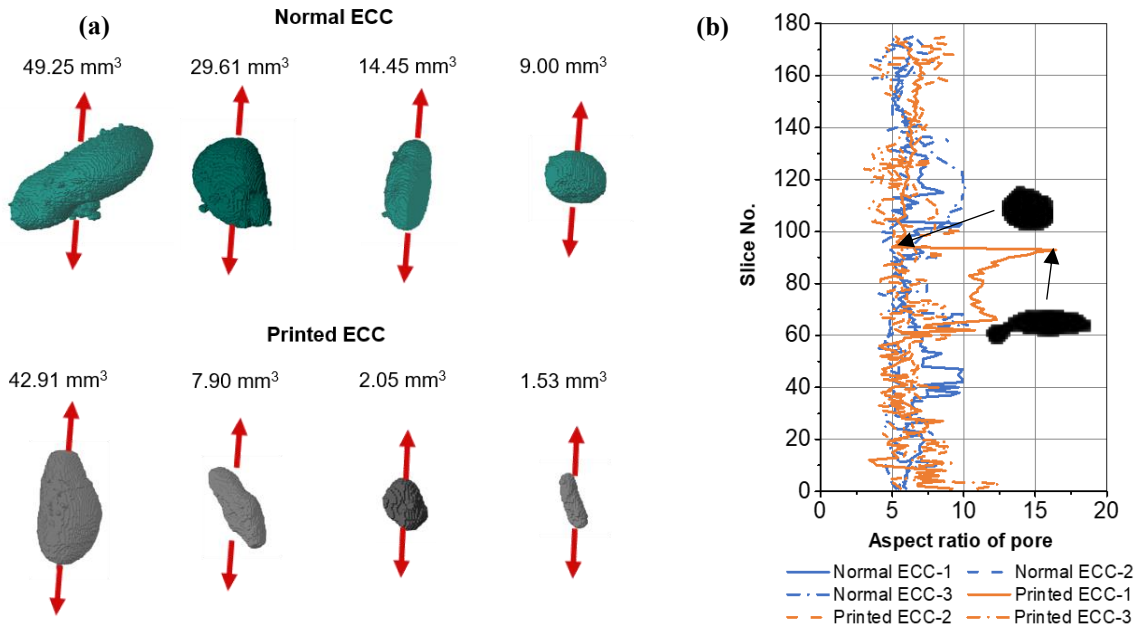

Fig. 17. (a) Typical shape of large pores; (b) Pore aspect ratio throughout normal and printed ECC.

3.4. Fibre orientation and dispersion

3.4.1 Fibre orientation

In terms of fibres, the heterogeneous microstructure of ECC contains variable localised fibre orientation distribution, length distribution and volume fraction. Due to the same fibre specifications for both mould cast and printed ECC specimens, the effects of variations in fibre orientation and dispersion on macroscopic tensile ductility are explored here. **Fig. 18** shows the BSE images of cross sections of normal ECC and printed ECC, where the unhydrated cement particles, epoxy impregnated pores and fibres were presented in black while the quartz sand was shown in grey. Compared to normal ECC, printed ECC had a more uniform fibre dispersion and the fibre orientation in it was more perpendicular to the direction of tension. To determine the fibre characteristics in ECC produced by different fabrication methods, the image processing approach introduced in Section 2.3.4 was adopted to analyse the fibre orientation and dispersion using the obtained BSE images.

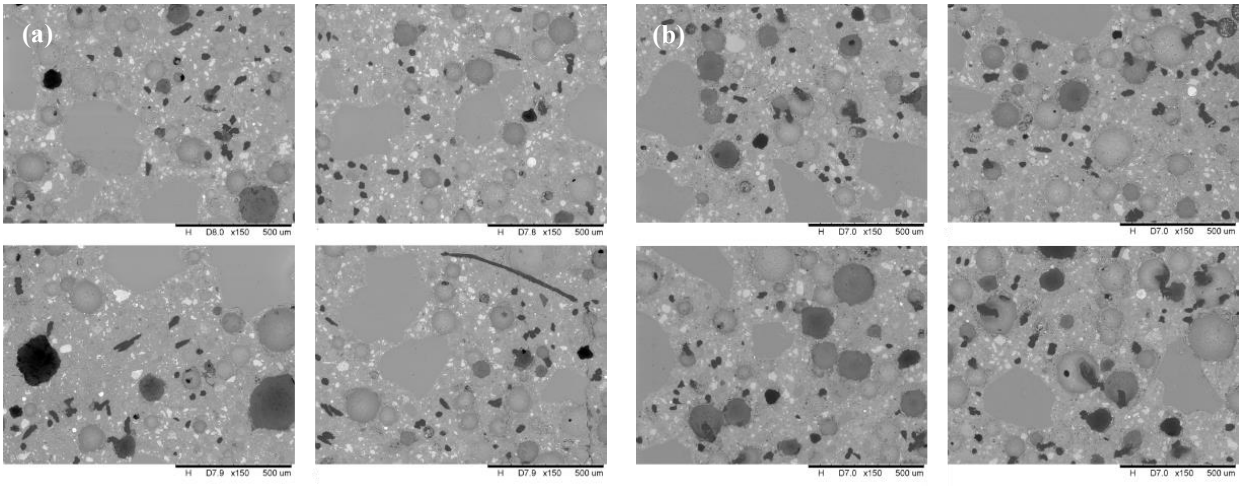

Fig. 18. BSE images of (a)normal ECC and (b) printed ECC with various orientation distribution.

Fig. 19 illustrates the frequency histograms and the corresponding cumulative frequency of fibre inclination angle θ, as well as the pie charts of fibre inclination angle θ. In general, most fibre inclination distribution of the cast ECC specimens tended to possess a larger angle compared to that in the printed ECC specimens. For instance, most fibre inclination angles of normal ECC specimens were within the range of 40-50°, 50-60°, and 50-60°, with the corresponding proportions of 33.6%, 36.2%, and 37.2%, respectively. It also can be observed that most of the fibre inclination angles of the printed specimens were concentrated in 30-40°, 30-40°, and 20-30°, with the corresponding proportions of 36.9%, 28.3%, and 28.7%, respectively. Moreover, when comparing the percentage of fibres with an inclination angle greater than 50°, the normal specimens had a value of 39.2%, 46.9%, and 50.7%, respectively, while the printed specimens had a value of 3.8%, 7.5%, and 4.7%, respectively, suggesting that the average value of fibre inclination angle over 50° for normal ECC was approximately 8.6 times that of printed ECC.

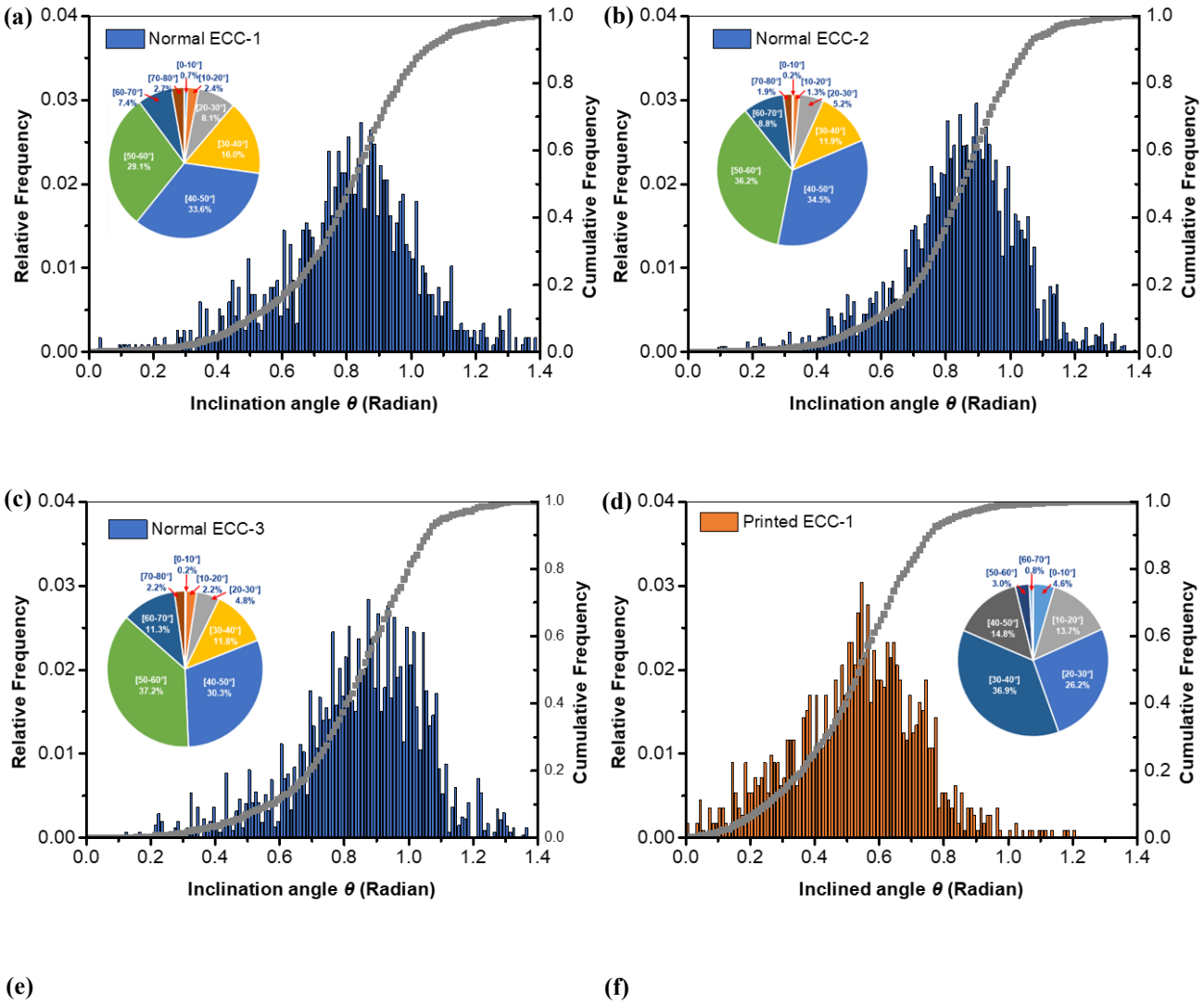

(e) (f)

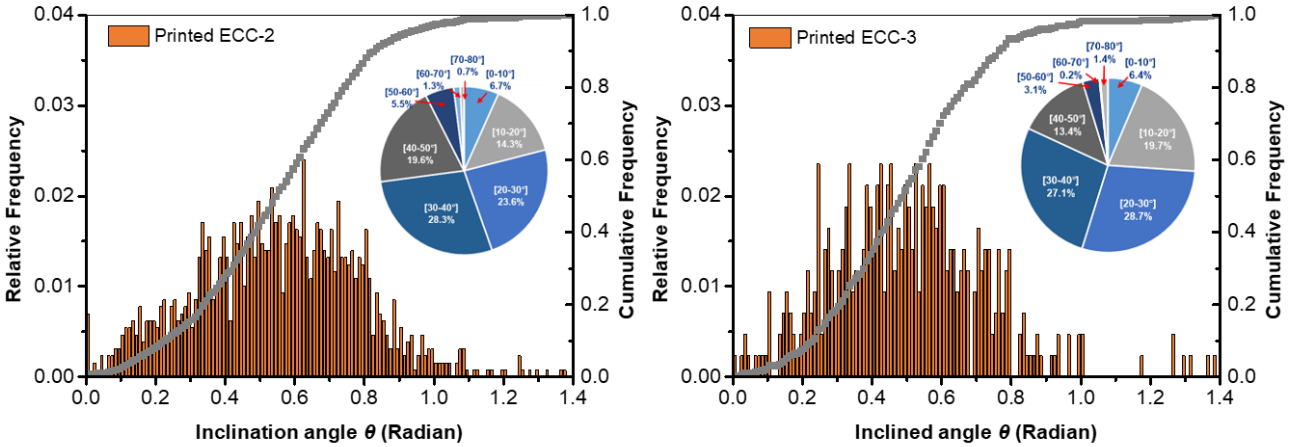

Fig. 19. Frequency and cumulative frequency of fibre inclination angle θ of (a) normal ECC-1, (b) normal ECC-2, (c) normal ECC-3, (d) printed ECC-1, (e) printed ECC-2, and (f) printed ECC-3.

According to the calculated inclination angle data, the practical distribution of fibre angles can be fitted by Eq. (6), and parameters r and q can be derived. **Fig. 20** shows the fitted probability density functions of fibre inclination angle θ for different specimens. **Table 6** presents the experimental and fitted data of the fibre orientation characteristics using the method described in Section 2.3.4. The average θ of the normal ECC was 47.7°, which was approximately 58% higher than that of the printed ECC (30.2°). The larger the value of r, the more $p(\theta)$ tends to be distributed with a larger inclination angle (**Fig. 19c**), while the larger the value of q, the more $p(\theta)$ tends to be distributed with a smaller inclination angle (**Fig. 19d**). The extreme points of the fitted probability density function for normal ECC specimens were corresponding to inclination angles of 47.5°, 47.8°, and 49.6°, respectively, indicating that most of the PE fibres in normal ECC had inclination angles larger than 45°. Furthermore, the extreme points of the fitted probability density function for printed ECC specimens corresponded to inclination angles of 30.7°, 30.7°, and 26.6° respectively, suggesting that most of the PE fibres in printed ECC had inclination angles of lower than 45°. This is consistent with the average angle of fibre for different fabrication methods presented in **Table 6**. All these indicate that short PE fibres in extrusion-based 3D printed ECC exhibited a higher fibre alignment in the printing direction, i.e., the fibre orientation is more perpendicular to the direction of tension, than that in normal ECC, which can help enhance the efficiency of fibre bridging action. A relatively higher degree of fibre alignment in printed ECC can be attributed to the fibres under high shear and compression forces tending to orient in the flow direction of ECC, i.e., the printing direction, which is in good agreement with the findings for 3D printed fibre-reinforced cementitious composites reported in Refs. [59, 101].

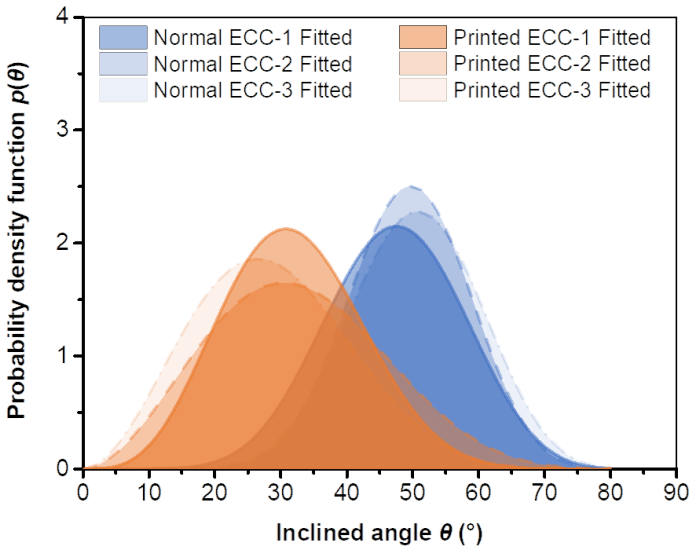

Fig. 20. Fitted probability density functions of fibre inclination angle θ of normal and printed ECC.

Table 6. Experimental and fitted data of the fibre orientation characteristics in ECC.

Sample	Experimental data		Fitting results	
	Average angle θ	Major distribution & proportion	r	q
Normal ECC-1	46.1°	[40-50°], 33.6%	4.1	3.5
Normal ECC-2	48.2°	[50-60°], 36.2%	5.1	3.5
Normal ECC-3	48.7°	[50-60°], 37.2%	5.9	4.4
Average	47.7°	-	5.0	3.8
Printed ECC-1	30.4°	[30-40°], 36.9%	2.2	5.3
Printed ECC-2	31.5°	[30-40°], 28.3%	1.4	3.2
Printed ECC-3	28.7°	[20-30°], 28.7%	1.4	4.3
Average	30.2	-	1.7	4.3

3.4.2 Fibre dispersion

In addition to the fibre orientation distribution, the fibre dispersion can also affect the fibre bridging effect at the crack opening. The local fibre content and fibre distribution coefficient, as described in Section 2.3.4, are used to quantify the distribution of PE fibres in the cutting ECC plane. It is worth noting that the local fibre content denotes the percentage of total fibre area on each piece. A comparison of the local fibre content and fibre distribution coefficient of normal ECC and printed ECC is presented in **Fig. 21a** and **b**, respectively. No apparent difference can be observed in terms of the average local fibre content in normal ECC and printed ECC. The local fibre content of printed ECC was slightly reduced from 2.42% to 2.37%. Moreover, both normal ECC and printed ECC were highly volatile. Besides, the average fibre distribution coefficient was found to be 0.82 for printed ECC, which was approximately 7.9% higher than normal ECC. This suggests that compared to normal ECC, the printed ECC had a relatively more uniform fibre distribution and the extrusion-based 3D concrete printing process for ECC may have no considerable influence on the fibre distribution in comparison with the normal production process.

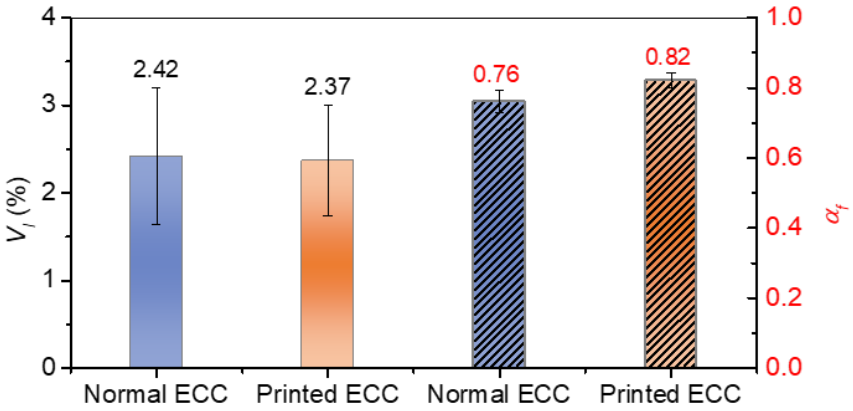

Fig. 21. Local fibre content and fibre distribution coefficient of normal and printed ECC.

4. Discussion

4.1 General

According to the micromechanics-based design theory of ECC, the strength and energy criteria given in Eqs. (10) and (11) should be satisfied to attain the tensile strain-hardening and multiple cracking behaviour [102]. Regarding the strength criterion, the composite cracking strength (σ_c) must not exceed the fibre-bridging stress (σ_b) crossing the crack, which controls the initiation of cracks in ECC. The energy criterion is set to govern the crack propagation mode that the crack tip toughness (J_{tip}) should be less than the complementary energy (J_b'), which can be calculated from the fibre bridge stress - crack opening (σ - δ) curve.

$$\sigma_c \leq \sigma_b \tag{10}$$

$$J_{tip} = \sigma_{ss}\delta_{ss} - \int_0^{\delta_{ss}} \sigma(\delta)d\delta = K_m^2/E_m \leq J_b' = \sigma_0\delta_0 - \int_0^{\delta_0} \sigma(\delta)d\delta \tag{11}$$

where δ_0 is the crack opening at the maximum bridging stress (σ_0), δ_{ss} is the crack opening corresponding to the steady state bridging stress (σ_{ss}), K_m is the fracture toughness of matrix that is equal to 0.118 MPa·m$^{1/2}$ for normal ECC and printed ECC derived by fitting the experimental data of direct tensile tests on ECC without fibre to Eq. (12), and E_m is the elastic modulus of matrix obtained from the stress-strain curve under uniaxial compression (18 GPa for both normal and printed ECC in this study).

$$\sigma_c = \frac{K_m}{2}\sqrt{\frac{\pi}{c}} \tag{12}$$

In addition, the pseudo-strain hardening (PSH) indices including $PSH_{strength}$ ($PSH_{strength} = \sigma_{tu}/\sigma_{tc}$) and PSH_{energy} ($PSH_{energy} = J_b'/J_{tip}$) were used to quantify the margin of the tensile ductility robustness [103]. In practice, $\sigma_0/\sigma_c \geq 1.3$ and $J_b'/J_{tip} \geq 2.7$ are needed to attain robust tensile strain-hardening.

Based on the first cracking strength and ultimate tensile strength given in **Table 5**, the average $PSH_{strength}$ of the normal and printed ECC corresponding to the stress level at first cracking was found to be 2.17 and 2.25, respectively, which exceeded 1.3, suggesting that both normal and printed ECC

can exhibit multiple cracking and strain-hardening behaviour. Single-crack tests on notched normal ECC and printed ECC specimens under direct tension (see **Fig. 22**) were conducted to obtain the bridging stress-crack opening relationship (σ-δ curve) and validate the strain-hardening behaviour.

Fig. 23a displays a typical σ-δ curve for ECC, which can be adopted to estimate the relationship between micro-scale material parameters and macro-scale tensile strain-hardening behaviour. The tensile stress-crack opening curves of normal and printed ECC obtained from the single crack tests were presented in **Fig. 23b**, indicating that the printed ECC has a greater average σ_0 than normal ECC with a small variation. The average crack opening (δ_0) of normal ECC measured at the notched sections of five specimens was 0.23 μm, which was slightly smaller than that of printed ECC (i.e., 0.25 μm). The complementary energy (J_b') of normal ECC and printed ECC calculated from the σ-δ curve was 265.02±38.55 J/m^2 and 337.06±31.03 J/m^2, respectively. The average value of J_b' of printed ECC with smaller fibre inclination angle was about 127% greater than that of normal ECC. The average value of J_{tip} derived using Eq. (11) was 0.77 J/m^2 for normal and printed ECC, implying that the toughness of matrix was low and thus would facilitate the steady-state cracking under constant applied stress. With the obtained J_b' and J_{tip}, the average values of PSH_e ($= J_b'/J_{tip}$) of normal and printed ECC can be calculated as 344.18 and 437.74, respectively, which fully satisfied the energy criterion. PSH_e is highly associated with tensile strain capacity. A higher PSH_e is favourable for more saturated cracking and leads to higher tensile strain capacity [104, 105], which suggests the printed ECC had a higher tensile stain capacity and more saturated cracking behaviour compared to normal ECC.

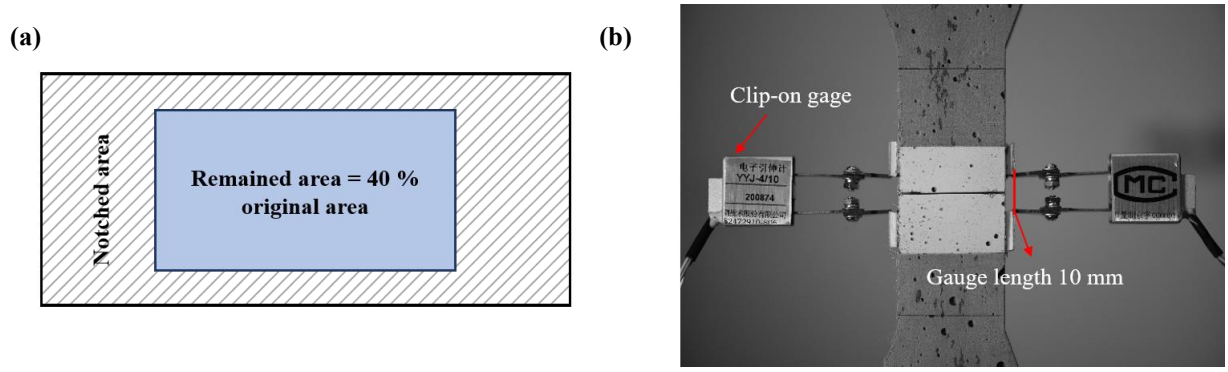

Fig. 22. Single-crack direct tension test: (a) notched dog-bone area and (b) test set up.

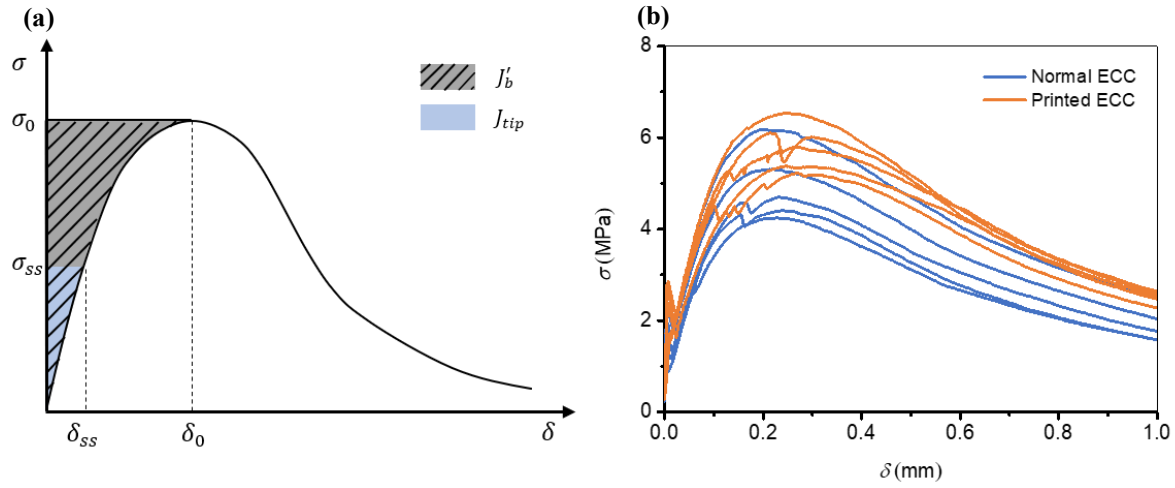

Fig. 23. (a) Typical σ-δ relation for strain-hardening cementitious composites (modified from [34]); (b) σ-δ relation for normal ECC and printed ECC.

4.2 Effect of pore structure characteristics on strain-hardening behaviour

The pore structure characteristics of ECC can significantly affect its tensile properties and the pore size distribution determines the number of cracks that can develop before the stress reaches the ultimate tensile strength [106]. Herein, the available model about the crack strength of composites containing short random fibres was firstly reviewed. Then, a simplified analytical model was proposed, assuming that the pores in matrix are not bridged by fibres initially. Afterwards, the analytical model was validated with experimental data including nominal pore size and cracking strength, where the nominal pore size was determined by the semi-major axis length (D_{max}/2) of the largest pore in this study.

Fig. 24 shows the BSE images of specimens cut from ECC specimens before uniaxial tensile test. Microcracks around the pores and along the interface between the sand and the matrix can be seen in both normal and printed ECC, which can be attributed to the dry shrinkage since both normal and printed ECC were cured in natural air condition. Internal pores and the sand/matrix interface are the origins of crack initiation and growth [96, 107, 108]. Cracks can form along microcracks around the fibres when subjected to tensile stress.

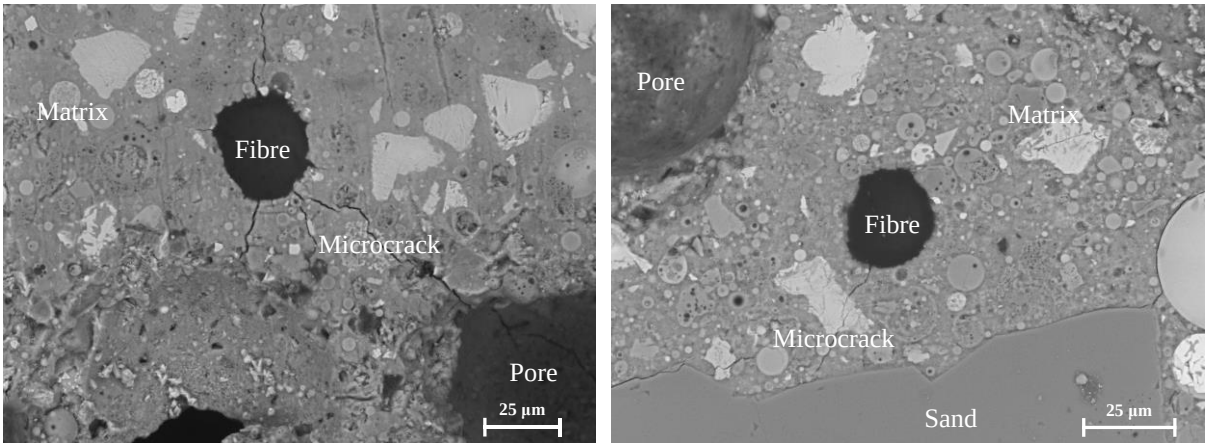

Fig. 24. Microcracks in ECC specimens before uniaxial tensile test.

Fig. 25a illustrates the analytical models for determining the crack strength of ECC containing randomly oriented short fibres. For a penny-shaped crack (the largest pore on each cross-section) bridged by fibres at the initial state, a parabolic crack was assumed to have uniform crack-bridging stress on the crack flanks, and the crack tip fracture toughness (K_{tip}) is the sum of the components related to the applied tensile load (K_L) and the fibre bridging (K_B) [102] as follows:

$$K_{tip} = K_L + K_B = \frac{E_c}{E_m} K_m \tag{13}$$

$$K_{tip} = 2\sqrt{\frac{c}{\pi}} \int_0^1 \frac{[\sigma_L - \sigma_B(\delta(X))]XdX}{\sqrt{1-X^2}} = 2\sqrt{\frac{c}{\pi}} \int_0^1 \frac{\sigma_L XdX}{\sqrt{1-X^2}} - 2\sqrt{\frac{c}{\pi}} \int_0^1 \frac{\sigma_B(\delta(X))XdX}{\sqrt{1-X^2}} \tag{14}$$

where c is the crack (pore) size, E_c is the elastic modulus of the composite, $X = x/c$ with x being the distance from a point on the crack surface (in the direction of crack growth) to the centre of the full crack or the opening edge of the half crack, and K_{tip} can be simply regarded as K_m for the composite with low fibre content.

In Eq. (14), the fibre bridging stress (σ_B) is directly associated with the crack opening displacement $\delta(x)$, as follows [109]:

$$\delta(x) = \sqrt{\frac{c}{\pi}} \frac{4(1-\nu^2)K_{tip}}{E_c} \sqrt{1 - \left(\frac{x}{c}\right)^2} \tag{15}$$

where ν is the Poisson's ratio of matrix, and $E_c = E_m V_m + E_f V_f$ with V_m denoting the volume fraction of matrix and E_f and V_f representing the elastic modulus and volume fraction of fibre, respectively.

Combining Eqs. (13)-(15) and setting $K_{tip} = K_m$, the crack strength (σ_c) of the section with bridging fibres can be calculated as:

$$\sigma_c = g\sigma_0 \left[\frac{\sqrt{\pi}}{2}\frac{\bar{K}}{\bar{C}} + \left(\frac{4}{3}\sqrt{\bar{C}} - \frac{1}{2}\bar{C}\right)\right] \tag{16}$$

with

$$g = 2\left(1 + e^{\pi f/2}\right)/(4 + f^2) \tag{17}$$

$$\sigma_0 = V_f \tau \left(l_f/d_f\right)/2 \tag{18}$$

$$\bar{K} = \left(K_{tip}/\sigma_0\sqrt{c_0}\right)/\left(g\tilde{\delta}^*\right) \tag{19}$$

$$\bar{C} = {\tilde{\delta}^*}^{-1}\sqrt{c/c_0} \tag{20}$$

$$c_0 = \left(\frac{l_f E_m}{2K_m}\right)^2 \frac{\pi}{16(1-\nu^2)^2} \tag{21}$$

$$\tilde{\delta}^* = \left(2\tau/E_f(1+\eta)\right)\left(l_f/d_f\right) \tag{22}$$

$$\eta = \left(V_f E_f\right)/(V_m E_m) \tag{23}$$

where $\bar{K}$ is the ratio of crack tip energy absorption to the energy absorbed by the fibre, $\bar{C}$ is the normalized crack radius at the peak-crack bridging displacement, f is the snubbing coefficient, τ is the interface frictional bond strength, and l_f and d_f are the length and diameter of fibre.

Once the included micromechanical parameters are given, the relation between crack strength and pore size can be determined by solving Eq. (16) which describes the contributions of matrix and fibres to the crack strength of ECC. As seen in the BSE images above, most pores were not bridged by fibres, which was also reported in Ref. [56]. Microcracks in the matrix around pores or sand can act as a path for crack growth. As the applied tensile load increases, the crack would propagate towards the fibres, while the fibres start taking the effect to inhibit the crack growth. For the case that the pores are not bridged by fibres, the analytical model for crack strength can be modified as illustrated in **Fig. 25b**, which is also composed of two parts with a minor change on K_L. For the integral variable x, the range of integration for calculating K_B remains [0, c], while for calculating K_L it is in the range of [0, $c + c_p$], where c_p is the nominal size of the initial pore without fibre across it and c is the crack size bridged by fibres during crack growth. In the original models, it was assumed that the crack shape during crack growth is related to the stress balance on the crack surface. As the cracks in the modified model are newly generated and the initial defects do not affect the initial crack opening displacement, such assumption is also valid for the modified model which can be calculated as a function of c and c_p as follows:

$$\sigma_c(c, c_p) = g\sigma_0 \left[\frac{\sqrt{\pi}}{2} \frac{\bar{K}}{\tilde{\delta}^{*-1} \sqrt{(c+c_p)/c_0}} + \left(\frac{4}{3}\sqrt{\bar{C}} - \frac{1}{2}\bar{C} \right) \right] \tag{24}$$

Fig. 26 shows the calculated crack strength with the input parameters listed in **Table 7** considering the nominal pore size using the original and modified models, which was compared with the experimental data for normal and printed ECC. It can be observed that the crack strength decreased continuously with the increasing pore size. Compared to the original model, the modified model gave the results closer to the experimental data. It should be noted that each pre-existing nominal pore size (c_p) is corresponding to a crack strength curve. The slight increase in calculated crack strength indicates the positive bridging effect of fibres during the crack propagation process. In addition, the crack strength provided by the matrix decreased with the increase of c_p. Hence, the peak crack strength corresponding to each pre-existing nominal pore size c_p forms the curves obtained using the modified model. E_m and τ are the key parameters for the calculations, the mean values of which were used in this study. Different production processes (mechanical vibrations and extrusion pressure) and curing conditions adopted for normal ECC and printed ECC can lead to variations in E_m and τ. Therefore, accurate measurement of input parameters, especially E_m and τ for normal and printed ECC can help further achieve precise predictions by the modified model.

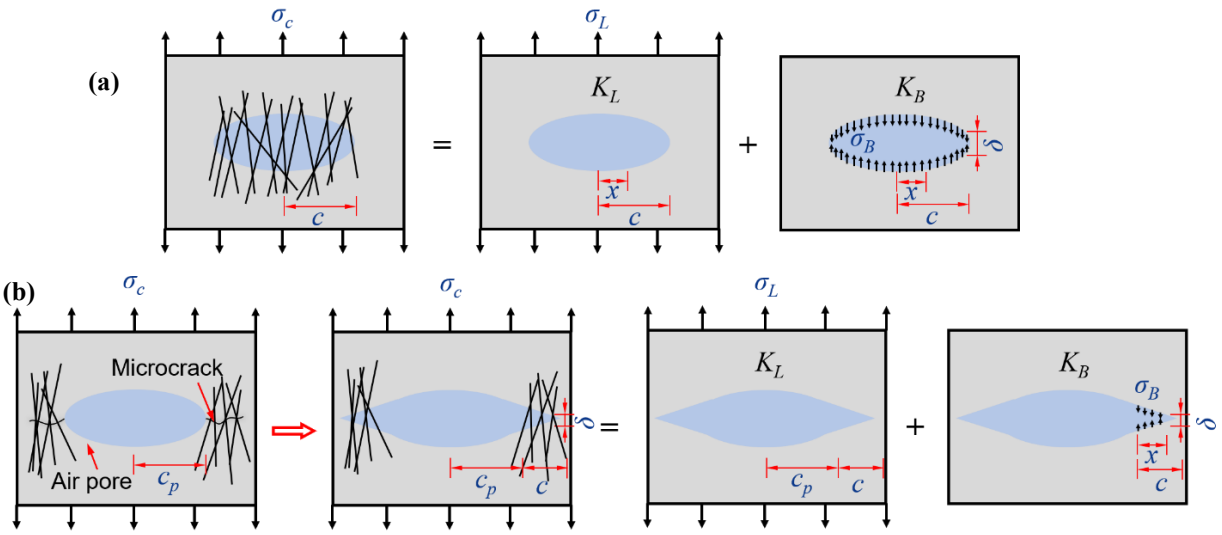

Fig. 25. Schematic illustration of the existing and modified models for determining the crack strength of ECC: (a) existing model and (b) modified model.

Table 7. Micromechanical parameters of ECC used as model input.

Fibre	Volume fraction, V_f	2%
	Length, l_f (mm)	6 and 12
	Diameter, d_f (mm)	0.024
	Elastic modulus, E_f (GPa)	110
	Tensile strength, σ_{fu} (MPa)	3000
	Interfacial chemical bond, G_d (J/m^2)	0
Matrix	Volume fraction, V_m	98%
	Elastic modulus, E_m (GPa)	18
	Fracture toughness, K_{tip} (MPa·m$^{1/2}$)	0.118
	Poisson's ratio, v	0.2
Fibre-matrix interface	Frictional bond, τ (MPa)	1.16
	Snubbing coefficient, f	0.65
	Fiber strength reduction factor, f'	0.50

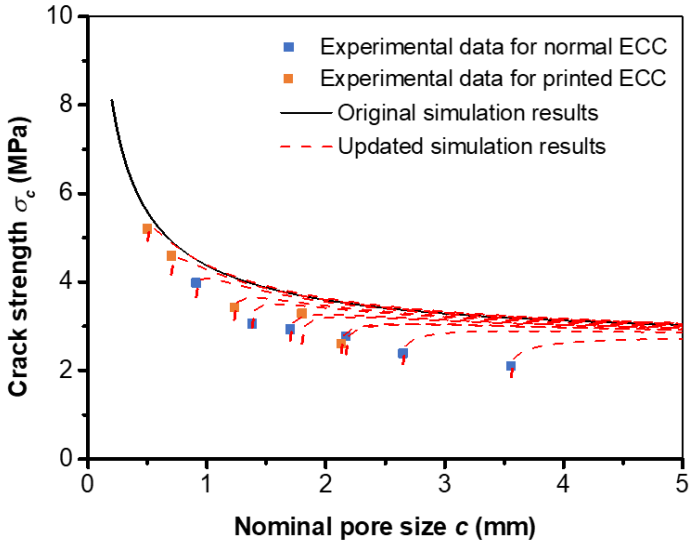

Fig. 26. Relationship between crack strength and nominal pore size for normal and printed ECC.

4.3 Effect of fibre characteristics on strain-hardening behaviour

The addition of viscosity modifier (HPMC) and the use of different manufacturing methods for ECC (mould casting and 3D printing) may affect the fibre dispersion and orientation in the fresh mixture, leading to variations in cracking-bridge capacities of the fibres in hardened ECC. According to the composite theory [81, 110], the ultimate tensile strength of ECC can be calculated considering the tensile strength of ECC matrix and fibre bridging effect as follows:

$$\sigma_{ct} = \eta_l \eta_\theta V_f \sigma_{fu} + (1 - V_f)\sigma_{mu} \quad (25)$$

$$\eta_\theta = \int_{\theta_{min}}^{\theta_{max}} p(\theta) cos^2\theta d\theta \quad (26)$$

where σ_{ct} is the ultimate tensile strength of the ECC (MPa), σ_{mu} is the tensile strength of the matrix (MPa), η_l is the coefficient related to the fibre length, η_θ is the fibre orientation coefficient, V_f is the fibre volume fraction, σ_{fu} is the fibre tensile strength (MPa), and $p(\theta)$ is the probability density function of the fibre orientation.

As indicated in Eq. (26), η_θ= 1 when all fibres are aligned parallel to the tensile stress direction, while η_θ= 0 implies that all fibres are aligned perpendicular to the tensile stress direction. Due to the similar matrix cracking strength of normal and printed ECC, only the effect of fibre orientation needs to be considered. By substituting the mean values of fibre orientation parameters *r* and *q* into Eq. (25), the fibre orientation coefficient for normal and printed ECC can be calculated as 0.432 and 0.717, respectively. The local fibre content and fibre dispersion of printed ECC are higher than those of normal ECC. These resulted in the higher ultimate tensile strength of printed ECC (5.40 MPa) than normal ECC (4.79 MPa), as presented in **Table 5**.

To investigate the effect of inclined angle θ on the strain-hardening behaviour of normal and printed ECC in terms of fibre pull-out from matrix, the probability of fibre rupture was further quantitatively analysed. According to [111, 112], the fibre rupture zone due to the aggregation of all potential rupture fibres can be derived by the critical ruptured length $l_d(\theta)$ and the fibre inclined angle θ, which can be expressed as Eq. (27). With the input parameters listed in **Table 7**, the fibre crack zone can be derived by substituting the mean value of fibre orientation parameters *r* and *q* into Eq. (7), which is displayed in **Fig. 27** along with the cumulative frequency of fibres in normal and printed ECC. Only when the fibre embedment length (l_e) is greater than $l_d(\theta)$, the fibre fracture can occur, which is highly dependent on the actual fibre embedment length. Furthermore, a critical angle (θ_c) can be derived as the minimum fibre inclined angle using Eq. (28). If the inclined angle is smaller than θ_c, the fibre would not rupture, regardless of the fibre embedment length.

$$l_d(\theta) = \frac{\sigma_{fu} d_f}{4\tau} e^{-(f+f')\theta} \quad (27)$$

$$\theta_c = -\frac{1}{f+f'} ln\left(\frac{2\tau l_f}{\sigma_{fu} d_f}\right) \quad (28)$$

As mentioned above, 1.5 vol% 6 mm and 0.5 vol% 12 mm short PE fibres were added into ECC. Here, the fibre rupture zones corresponding to different fibre lengths were described separately. The inclination angle of most fibres was less than the critical angle (81.9°) when the fibre embedded length was 3 mm (half of the fibre length of 6 mm), suggesting that most fibres would be pulled out from the matrix during crack propagation. Therefore, the effect of 6 mm fibre fracture on bridging capacity can be ignored. In addition, the critical angle was 47.3° when the embedded length was 6 mm (half of the fibre length of 12 mm). 57.5% of the fibres (i.e., 0.2875 vol% 12 mm fibres) were at risk of fracture for normal ECC, while that fibre content for printed ECC was only 8.8% (i.e., 0.044 vol% 12 mm fibres), implying that printed ECC would present a higher fibre-bridging action than normal ECC given the local fibre content and fibre dispersion. No apparent difference can be observed in terms of the fibre content at risk of rupture due to small addition of 12 mm PE fibres (0.5 vol%), which suggests that premature fibre failure has little effect on the calculation of fibre bridging stress at a given cross-section for normal and printed ECC studied herein. This is consistent with the test results in terms of average maximum bridging stress (σ_0) which was 4.97 MPa and 5.80 MPa respectively for normal and printed ECC. However, for ECCs produced with 100% 12 mm or longer fibres, the effect of fibre fracture on crack-bridging strength will play more significant roles. Moreover, as the same fibres are used for normal and printed ECC, it can also be found from Eq. (27) that the critical ruptured length ($l_d(\theta)$) is also influenced by the interfacial frictional bonding strength (τ) besides the snubbing coefficient (f) and the fibre strength reduction coefficient (f'). The bond strength between the fibres and the matrix of normal and printed ECC may be different due to the different production methods. The critical fracture inclination corresponding to the same embedment length was reduced with the increase of the bond strength, leading to a further increase in the risk of fibre rupture. Thus, a quantitative assessment of the fibre rupture effect is required for calculating the fibre bridging stress, which can help obtain an accurate prediction result.

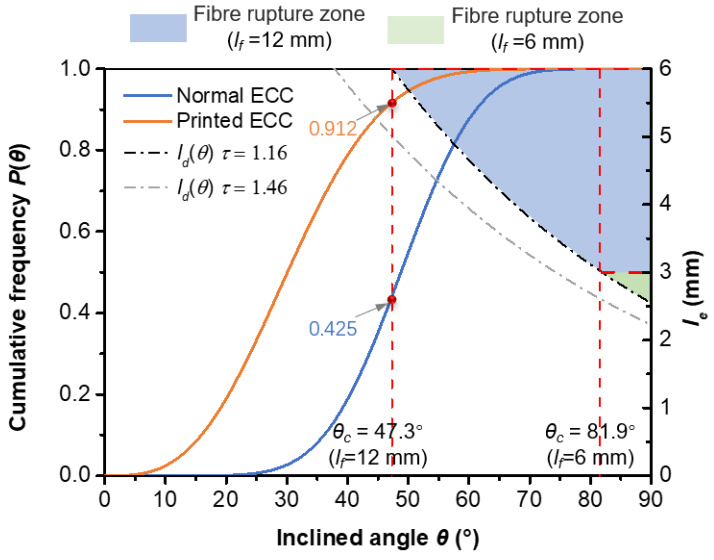

Fig. 27. Comparation of fibre rupture zone for normal and printed ECC.

Based on the analysis and discussion above, it can be concluded that the matrix in normal ECC had a higher probability of large pores than that in printed ECC, leading to an increase in the risk of damage localization and more variation in tensile properties, while there is little difference in pore shape property between normal ECC and printed ECC. If ignoring the pore size difference between normal and printed specimens, the difference in tensile properties of them can be mainly ascribed to the fibre orientation and distribution. **Fig. 28** illustrates the fibre-bridging action of normal ECC and printed ECC in tension. For a given crack opening, normal ECC with a higher inclination angle exhibits a weaker fibre bridging stress. When fibres are loaded at an excessive inclination angle, the in-situ tensile strength of fibres may be reduced due to fibre surface abrasion, local bending, and lateral stress, resulting in premature fibre rupture during the slip-hardening process [113]. Moreover, the fibres with higher inclination angles may induce matrix spalling at the exit point of the fibres in normal-strength ECC, leading to a reduction in effective embedment length and pull-out resistance [114]. Besides, a lower fibre distribution coefficient would increase the risk of fibre coagulation, which in turn reduces the fibre-bridging ability to resist crack opening.

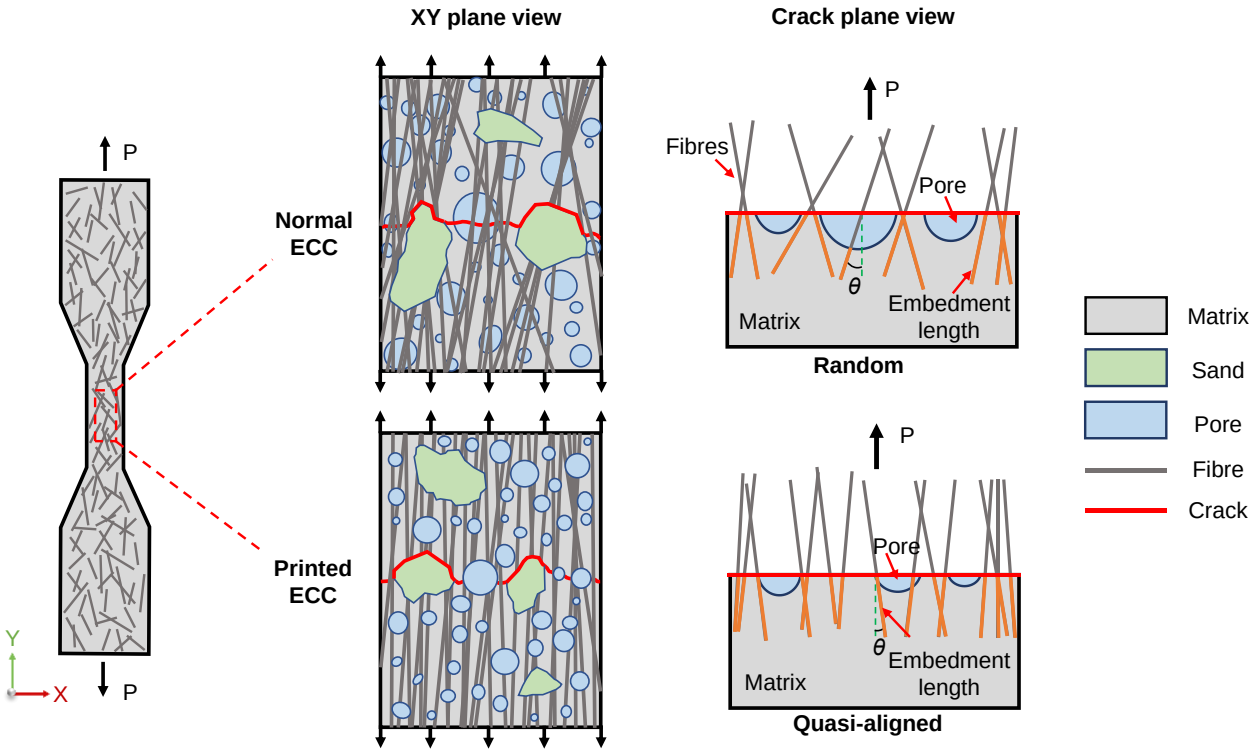

Fig. 28. Illustration of fibre bridge action of normal and printed ECC in tension.

5. Conclusions

In this study, a comparison of the pore structure features, fibre characteristics and strain-hardening behaviour of ECC reinforced with 6 and 12 mm PE fibres manufactured by extrusion-based 3D concrete printing and mould casting was conducted, aiming to better understand the relationship between microstructure and tensile strain-hardening behaviour of 3D printed ECC. Based on the experimental results and theoretical analysis, the main conclusions can be drawn as follows:

(1) The compressive strength of mould cast ECC declined with the increase of fibre length. The normal ECC mixture with 100% 6 mm fibres exhibited the highest compressive strength, i.e., 61.03 MPa. The compressive strength of printed ECC under z-direction of loading was 4% higher than that of normal ECC, which can be attributed to the continuous extrusion pressure and larger contact area between filaments.

(2) No obvious difference can be observed for the 28-d first cracking strength of all ECC specimens. Normal ECC and printed ECC with the same thickness of 15 mm had comparable tensile properties. However, the ultimate tensile strength and tensile strain capacity of printed ECC specimen (3DP-L6+12-T15) were found to be 12.7% and 9.4% respectively higher than that of normal ECC specimen (N-L6+12-T30), suggesting that more robust composite ductility can be achieved by the extrusion-based 3D printing process. The block specimens with uniform 3D distribution of fibres for mould casting can be used to compare the tensile properties of cast-in-situ and printed ECC specimens. Additionally, considering both printability and basic mechanical properties, the feasibility of 3D printed plane ECC (1.5 vol% 6 mm and 0.5 vol% 12 mm fibres) with unique tensile ductility (above 5%), autogenous crack width control (less than 100 μm), and compressive strength of over 50 MPa was experimentally verified based on extrusion-based 3D printing.

(3) Normal ECC tended to have more large pores compared to printed ECC, leading to larger variations in tensile properties. As an important feature of pore shape, a similar aspect ratio of pores ranging from 5-10 can be observed for normal and printed ECC, implying that the pore morphology in a single printed filament is nearly identical to that in normal ECC. The average aspect ratio of pores in normal ECC specimens was 6.52%, 5.72%, and 6.33%, respectively, while that in printed ECC specimens was 7.01%, 6.62%, and 5.73%, respectively.

(4) Short fibres in extrusion-based 3D printed ECC exhibited a higher fibre alignment in the printing direction, i.e., the fibre orientation is more perpendicular to the tensile loading direction compared to that in normal ECC. There did not exist a close correlation between fibre distribution characteristics (local fibre volume fraction and fibre distribution coefficient) and manufacturing method (mould-casting and extrusion-based 3D printing). The fibre inclination angle for normal ECC was 47.7°, which was approximately 58% higher than that for printed ECC. Specifically, the number of fibre inclination angles over 50° for normal ECC was about 8.6 times that for printed ECC. The local fibre content for normal and printed ECC was 2.42% and 2.37%, respectively. The average fibre distribution coefficient for printed ECC was 0.82, which was about 7.9% higher than that for normal ECC.

(5) Both strength and energy criteria for tailoring ECC were successfully satisfied, which guarantees the tensile strain-hardening behaviour in normal and printed ECC. A modified analytical model for predicting the crack strength of ECC was proposed, which can predict the cracking

characteristics of normal and printed ECC with acceptable accuracy. The difference in tensile properties of normal ECC and printed ECC can be well explained by the micromechanics-based design criteria and the modified analytical model with different microstructure parameters as inputs, which can facilitate the optimisation of 3D printable ECC mix design and printing process.

Acknowledgements

This study was funded by the National Natural Science Foundation of China (No.52130210), Victoria-Jiangsu Innovation and Technology R&D Fund (BZ2020019), and China Scholarship Council (No.202006090274). M. Zhang gratefully acknowledges the financial support from the Engineering and Physical Sciences Research Council (EPSRC), UK under Grant No. EP/R041504/1 and the Royal Society, UK under Award No. IEC\NSFC\191417 as well as the Visiting Researcher Fund Program of State Key Laboratory of Water Resources and Hydropower Engineering Science, China under Award No. 2019SGG01.

References

[1] S. Lim, R.A. Buswell, T.T. Le, S.A. Austin, A.G.F. Gibb, T. Thorpe, Developments in construction-scale additive manufacturing processes, Automat. Constr., 21(1) (2012) 262-268.

[2] P. Wu, J. Wang, X.Y. Wang, A critical review of the use of 3-D printing in the construction industry, Automat. Constr., 68 (2016) 21-31.

[3] V. Mechtcherine, F.P. Bos, A. Perrot, W.R. Leal da Silva, V.N. Nerella, S. Fataei, R.J.M. Wolfs, M. Sonebi, N. Roussel, Extrusion-based additive manufacturing with cement-based materials-Production steps, processes, and their underlying physics: A review, Cement Concr. Res., 132 (2020) 106037.

[4] K. Vallurupalli, N. Farzadnia, K.H. Khayat, Effect of flow behavior and process-induced variations on shape stability of 3D printed elements - A review, Cement Concr. Compos., 118 (2021) 103952.

[5] T.A.M. Salet, Z.Y. Ahmed, F.P. Bos, H.L.M. Laagland, Design of a 3D printed concrete bridge by testing, Virtual. Phys. Prototy., 13(3) (2018) 222-36.

[6] Nijmegen has the longest 3D-printed concrete bicycle bridge in the world, https://www.tue.nl/en/news-and-events/news-overview/01-01-1970-nijmegen-has-the-longest-3d-printed-concrete-bicycle-bridge-in-the-world/, Accessed 13th Oct 2021.

[7] A. Anton, L.R.T. Wangler, V. Frangez, R.J. Flatt, B. Dillenburger, A 3D concrete printing prefabrication platform for bespoke columns, Autom. Constr., 122 (2021) 103467.

[8] Y.W. Weng, M.Y. Li, S.Q. Ruan, T.N. Wong, M.J. Tan, K.L.O. Yeong, S.Z. Qian, Comparative economic, environmental and productivity assessment of a concrete bathroom unit fabricated through 3D printing and a precast approach, J. Clean. Prod., 261 (2020) 121245.

[9] G.Vantyghem, W.D. Corte, E. Shakour, O. Amir, 3D printing of a post-tensioned concrete girder

designed by topology optimization, Autom. Constr., 112 (2020) 103084.

[10] OptiBridge: a topology optimized 3D-printed concrete bridge, https://www.ugent.be/ea/structural-engineering/en/research/clusters/themes/digitalfabrication/projectsdigitalfabrication/optibridge2.htm, Accessed 13th Oct 2021.

[11] Striatus, https://www.striatusbridge.com/, Accessed 13th Oct 2021.

[12] F.P. Bos, Z.Y. Ahmed, R.J.M. Wolfs, T.A.M. Salet, Experimental exploration of metal cable as reinforcement in 3D printed concrete, Materials., 10 (11) (2017) 1314].

[13] J.H. Lim, B. Panda, Q.C. Pham, Improving flexural characteristics of 3D printed geopolymer composites with in-process steel cable reinforcement, Constr. Build. Mater., 178 (2018) 32-41.

[14] Z.J. Li, L. Wang, G.W. Ma, Mechanical improvement of continuous steel microcable reinforced geopolymer composites for 3D printing subjected to different loading conditions, Compos. Part B-Eng., 187 (2020) 107796.

[15] V. Mechtcherine, A. Michel, M. Liebscher, T. Schmeier, Extrusion-Based additive manufacturing with carbon reinforced concrete: Concept and feasibility study, Materials, 13 (11) (2020) 2568.

[16] J.F., Caron, L. Demont, N. Ducoulombier, R. Mesnil, 3D printing of mortar with continuous fibres: Principle, properties and potential for application, Autom. Constr., 129 (2021) 103806.

[17] L. Demont, N. Ducoulombier, R. Mesnil, J.F. Caron, Flow-based pultrusion of continuous fibers for cement-based composite material and additive manufacturing: rheological and technological requirements, Compos. Struct., 262 (2021) 113564.

[18] L. Hass, F. Bos, Bending and pull-out tests on a novel screw type reinforcement for extrusion-based 3D printed concrete, 2nd RILEM International Conference on Concrete and Digital Fabrication, Springer, Cham (2020) 632-645.

[19] T. Marchment, J. Sanjayan, Bond properties of reinforcing bar penetrations in 3D concrete printing, Autom. Constr., 120 (2020) 103394.

[20] T. Marchment, J. Sanjayan, Lap Joint Reinforcement for 3D Concrete Printing, J. Struct. Eng., 148 (6) (2022) 04022063.

[21] L. Wang, G.W. Ma, T.H. Liu, R. Buswell, Z.J. Li, Interlayer reinforcement of 3D printed concrete by the in-process deposition of U-nails, Cem. Concr. Res., 148 (2021) 106535.

[22] X.Y. Sun, J.W. Zhou, Q. Wang, J.P. Shi, H.L. Wang, PVA fibre reinforced high-strength cementitious composite for 3D printing: Mechanical properties and durability, Addit. Manuf., 49 (2022) 102500.

[23] G.W. Ma, Z.J. Li, L. Wang, F. Wang, J. Sanjayan, Mechanical anisotropy of aligned fiber reinforced composite for extrusion-based 3D printing, Constr. Build. Mater., 202 (2019) 770-

783.

[24] F.P. Bos, E. Bosco, T.A.M. Salet, Ductility of 3D printed concrete reinforced with short straight steel fibers, Virtual. Phys. Prototyp., 14 (2019) 160-174.

[25] J.B. Sun, F. Aslani, J. Lu, L.N. Wang, Y.M. Huang, G.W. Ma, Fibre-reinforced lightweight engineered cementitious composites for 3D concrete printing, Ceram. Int., 47 (19) (2021) 27107-27121.

[26] V. Mechtcherine, R. Buswell, H. Kloft, F.P. Bos, N. Hack, R. Wolfs, J. Sanjayan, B. Nematollahi, E. Ivaniuk, T. Neef, Integrating reinforcement in digital fabrication with concrete: A review and classification framework, Cement Concr. Compos., 119 (2021) 103964.

[27] K.Q. Yu, L.Z. Li, J.T. Yu, J.Z. Xiao, J.H. Ye, Y.C. Wang, Feasibility of using ultra-high ductility cementitious composites for concrete structures without steel rebar, Eng. Struct., 170 (2018) 11-20.

[28] B.R. Zhu, J.L. Pan, Z.X. Zhou, J.M. Cai, Mechanical properties of engineered cementitious composites beams fabricated by extrusion-based 3D printing, Eng. Struct., 238 (2021) 112201.

[29] L. Xu, J.L. Pan, J.M. Cai, Seismic performance of precast RC and RC/ECC composite columns with grouted sleeve connections, Eng. Struct., 188 (2019) 104-110.

[30] M.J. Hou, K.X. Hu, J.T. Yu, S.W. Dong, S.L. Xu, Experimental study on ultra-high ductility cementitious composites applied to link slabs for jointless bridge decks, Compos. Struct., 204 (2018) 167-177.

[31] H. Zhu, T.Y. Wang, Y.C. Wang, V.C. Li, Trenchless rehabilitation for concrete pipelines of water infrastructure: A review from the structural perspective, Cement Concr. Compos., 123 (2021) 104193.

[32] J.S. Qiu, W.L. Aw-Yong, E.H. Yang, Effect of self-healing on fatigue of engineered cementitious composites (ECCs), Cement Concr. Compos., 94 (2018) 145-152.

[33] C. Schröfl, V. Mechtcherine, A. Kaestner, P. Vontobel, J. Hovind, E. Lehmann, Transport of water through strain-hardening cement-based composite (SHCC) applied on top of cracked reinforced concrete slabs with and without hydrophobization of cracks - Investigation by neutron radiography, Constr. Build. Mater., 76 (2015) 70-86.

[34] V.C. Li, Engineered Cementitious Composites (ECC): Bendable Concrete for Sustainable and Resilient Infrastructure, Springer, 2019.

[35] V.C. Li, H.C. Wu, Conditions for pseudo strain-hardening in fiber reinforced brittle matrix composites, Appl. Mech. Rev., 45(8) (1992) 390-398.

[36] D.G. Soltan, V.C. Li, A self-reinforced cementitious composite for building-scale 3D printing, Cement Concr. Compos., 90 (2018) 1-13.

[37] S.C. Figueiredo, C.R. Rodríguez, Z.Y. Ahmed, D.H. Bos, Y.D. Xu, T.M. Salet, O. Çopuroğlu, E.

Schlangen, F.P. Bos, An approach to develop printable strain hardening cementitious composites, Mater. Design., 169 (2019) 107651.

[38] K.Q. Yu, W. McGee, T.Y. Ng, H. Zhu, V.C. Li, 3D-printable engineered cementitious composites (3DP-ECC): Fresh and hardened properties, Cement Concr. Res., 143 (2021) 106388.

[39] J. Yu, C.K. Leung, Impact of 3D printing direction on mechanical performance of strain-hardening cementitious composite (SHCC), RILEM International Conference on Concrete and Digital Fabrication, Springer, Cham (2018) 255-265.

[40] Y. Bao, M. Xu, D. Soltan, T. Xia, A. Shih, H.L. Clack, V.C. Li, Three-dimensional printing multifunctional engineered cementitious composites (ECC) for structural elements, RILEM International Conference on Concrete and Digital Fabrication, Springer, Cham (2018) 115-128.

[41] H. Ogura, V.N. Nerella, V. Mechtcherine, Developing and testing of strain-hardening cement-based composites (SHCC) in the context of 3D-printing, Materials, 11(8) (2018) 1375.

[42] B.R. Zhu, J.L. Pan, B. Nematollahi, Z.X. Zhou, Y. Zhang, J. Sanjayan, Development of 3D printable engineered cementitious composites with ultra-high tensile ductility for digital construction, Mater. Des., 181 (2019), 108088.

[43] J.H. Ye, C. Cui, J.T. Yu, K.Q. Yu, F.Y. Dong, Effect of polyethylene fiber content on workability and mechanical-anisotropic properties of 3D printed ultra-high ductile concrete, Constr. Build. Mater., 281 (2021) 122586.

[44] J.H. Ye, C. Cui, J.T. Yu, K.Q. Yu, J.Z. Xiao, Fresh and anisotropic-mechanical properties of 3D printable ultra-high ductile concrete with crumb rubber, Compos. Part B Eng., 211 (2021) 108639.

[45] V.C. Li, C. Wu, S. Wang, A. Ogawa, T. Saito, Interface tailoring for strain hardening PVA-ECC, ACI Mater. J., 99 (2002) 463-472.

[46] J.G. Dai, B.T. Huang, S.P. Shah, Recent advances in strain-hardening uhpc with synthetic fibers, J. Compos. Sci., 10(5) (2021) 283.

[47] Y Ding, J Yu, KQ Yu, S Xu, Basic mechanical properties of ultra-high ductility cementitious composites: From 40 MPa to 120 MPa, Composite structures, 185 (2018) 634-645.

[48] K Yu, L Li, J Yu, Y Wang, J Ye, QF Xu, Direct tensile properties of engineered cementitious composites: A review, Construction and Building Materials, 165 (2018) 346-362.

[49] R.J.M. Wolfs, F.P. Bos, T.A.M. Salet, Hardened properties of 3D printed concrete: The influence of process parameters on interlayer adhesion, Cement Concr. Res., 119 (2019) 132-140.

[50] J.X. Li, J. Weng, E.H. Yang, Stochastic model of tensile behavior of strain-hardening cementitious composites (SHCCs), Cement Concr. Res., 124 (2019) 105856.

[51] J. Zhou, S.Z. Qian, G. Ye, O. Copuroglu, K.V. Breugel, V.C. Li, Improved fiber distribution and mechanical properties of engineered cementitious composites by adjusting the mixing sequence,

Cement Concr. Compos., 34(3) (2012) 342-348.

[52] M. Li, V.C. Li, Rheology, fiber dispersion, and robust properties of engineered cementitious composites, Mater. Struct., 46 (2013) 405-420.

[53] Y. Chen, O. Çopuroğlu, C.R. Rodriguez, F.F. de M. Filho, E. Schlangen, Characterization of air-void systems in 3D printed cementitious materials using optical image scanning and X-ray computed tomography, Mater. Charact., 173 (2021) 110948.

[54] J. Kruger, A. du Plessis, G. van Zijl, An investigation into the porosity of extrusion-based 3D printed concrete, Addit. Manuf., 37 (2021) 101740.

[55] S.W. Yu, M. Xia, J. Sanjayan, L. Yang, J.Z. Xiao, H.J. Du, Microstructural characterization of 3D printed concrete, J. Build. Eng., 44 (2021) 102948.

[56] C. Lu, V.C. Li, C.K.Y. Leung, Flaw characterization and correlation with cracking strength in Engineered Cementitious Composites (ECC), Cement Concr. Res., 107 (2018) 64-67.

[57] R. Lorenzoni, I. Curosu, F. Léonard, S. Paciornik, V. Mechtcherine, F.A. Silva, G. Bruno, Combined mechanical and 3D-microstructural analysis of strain-hardening cement-based composites (SHCC) by in-situ X-ray microtomography, Cement Concr. Res., 136 (2020) 106139.

[58] L.Y. Xu, B.T. Huang, V.C. Li, J.G. Dai, High-strength high-ductility Engineered/Strain-Hardening Cementitious Composites (ECC/SHCC) incorporating geopolymer fine aggregates, Cement Concr. Compos., 125 (2022) 104296.

[59] A.R. Arunothayan, B. Nematollahi, R. Ranade, S.H. Bong, J.G. Sanjayan, K.H. Khayat, Fiber orientation effects on ultra-high performance concrete formed by 3D printing, Cement Concr. Res., 143 (2021) 106384.

[60] P. Stähli, R. Custer, J.G.M. van Mier, On flow properties, fibre distribution, fibre orientation and flexural behaviour of FRC, Mater. Struct., 41 (2008) 189-196.

[61] B.Y. Lee, J.K. Kim, J.S. Kim, Y.Y. Kim, Quantitative evaluation technique of Polyvinyl Alcohol (PVA) fiber dispersion in engineered cementitious composites, Cement Concr. Compos., 31(6) (2009) 408-417.

[62] H.L Wu, J. Yu, D. Zhang, J.X. Zheng, V.C. Li, Effect of morphological parameters of natural sand on mechanical properties of engineered cementitious composites, Cement Concr. Compos., 100 (2019) 108-119.

[63] Y.X. Shao, S.P. Shah, Mechanical properties of PVA fiber reinforced cement composites fabricated by extrusion processing, ACI Mater. J., 94 (1997) 555-564.

[64] B. Felekoğlu, K. Tosun-Felekoğlu, E. Gödek, A novel method for the determination of polymeric micro-fiber distribution of cementitious composites exhibiting multiple cracking behavior under tensile loading, Constr. Build. Mater., 86 (2015) 85-94.

[65] M.Z. Wang, Y.S. Liu, B.M. Qi, D. Li, W. Wang, BSE-based dispersion quantification of carbon

fibres in cementitious composite through FCM-CA approach, Constr. Build. Mater., 260 (2020) 119789.

[66] C. Ding, L.P. Guo, B. Chen, Orientation distribution of polyvinyl alcohol fibers and its influence on bridging capacity and mechanical performances for high ductility cementitious composites, Constr. Build. Mater., 247 (2020) 118491.

[67] GB175-2007. Common portland cement, Beijing, Standards Press of China, 2007.

[68] GB/T 50146-2014. Technical code for application of fly ash concrete, Beijing, China Planning Press, 2015.

[69] GB/T 27690-2011. Silica fume for cement mortar and concrete, Beijing, Standards Press of China, 2012.

[70] N. Roussel, J. Spangenberg, J. Wallevik, R. Wolfs, Numerical simulations of concrete processing: From standard formative casting to additive manufacturing, Cement Concr. Res., 135 (2020) 106075.

[71] JC/T 2641-2018. Standard test method for the mechanical properties of ductile fibre reinforced cementitious composites, Beijing, China Building Materials Press, 2018.

[72] JSCE, Recommendations for Design and Construction of High Performance Fibre Reinforced Cement Composites with Multiple Fine Cracks, Japan Society of Civil Engineers, Tokyo, Japan, 2008, 1-16.

[73] J. Pourchez, B. Ruot, J. Debayle, E. Pourchez, P. Grosseau, Some aspects of cellulose ethers influence on water transport and porous structure of cement-based materials, Cement Concr. Res., 40(2) (2010) 242-252.

[74] S.C. Figueiredo, O. Çopuroğlu, E. Schlangen, Effect of viscosity modifier admixture on Portland cement paste hydration and microstructure, Constr. Build. Mater., 212 (2019) 818-840.

[75] A. Jenni, L. Holzer, R. Zurbriggen, M.Herwegh, Influence of polymers on microstructure and adhesive strength of cementitious tile adhesive mortars, Cement Concr. Res., 35(1) (2005) 35-50.

[76] Y. Chen, S.C. Figueiredo, Z.M. Li, Z. Chang, K. Jansen, O. Çopuroğlu, E. Schlangen, Improving printability of limestone-calcined clay-based cementitious materials by using viscosity-modifying admixture, Cement Concr. Res., 132 (2020) 106040.

[77] H.S. Wong, M.K. Head, N.R. Buenfeld, Pore segmentation of cement-based materials from backscattered electron images, Cement Concr. Res., 36 (6) (2006) 1083-1090.

[78] A Practical Guide to Microstructural Analysis of Cementitious Materials, Edited by Karen Scrivener, Ruben Snellings, Barbara Lothenbach. CRC Press, 2016.

[79] M. Xia, H. Hamada, Z. Maekawa, Flexural stiffness of injection molded glass fibre reinforced thermoplastics, Int. Polym. Process., 10 (1995) 74-81.

[80] K.T. Felekoğlu, B. Felekoğlu, R. Ranade, B.Y. Lee, V.C. Li, The role of flaw size and fiber distribution on tensile ductility of PVA-ECC, Compos. Part B Eng., 56 (2014) 536-545.

[81] L. Teng, W.N. Meng, K.H. Khayat, Rheology control of ultra-high-performance concrete made with different fiber contents, Cement Concr. Res., 138 (2010) 106222.

[82] C.P. Xie, M.L. Cao, W. Si, M. Khan, Experimental evaluation on fiber distribution characteristics and mechanical properties of calcium carbonate whisker modified hybrid fibers reinforced cementitious composites, Constr. Build. Mater., 265 (2020) 120292.

[83] T.F. Yuan, J.Y. Lee, Y.S. Yoon, Enhancing the tensile capacity of no-slump high-strength high-ductility concrete, Cement Concr. Compos., 106 (2020) 103458.

[84] N. Ranjbar, M. Zhang, Fiber-reinforced geopolymer composites: a review, Cement Concr. Compos., 107 (2020) 103498.

[85] K.Q. Yu, Y. Ding, Y.X. Zhang, Size effects on tensile properties and compressive strength of engineered cementitious composites, Cement Concr. Compos., 113 (2020) 103691.

[86] G.L. Xue, E. Yilmaz, W.D. Song, S. Cao, Fiber length effect on strength properties of polypropylene fiber reinforced cemented tailings backfill specimens with different sizes, Constr. Build. Mater., 241 (2020) 118113.

[87] J.Z. Xiao, H.R. Liu, T. Ding, Finite element analysis on the anisotropic behavior of 3D printed concrete under compression and flexure, Addit. Manuf., 39 (2021) 101712.

[88] H. Zhong, M.Z. Zhang, Effect of recycled tyre polymer fibre on engineering properties of sustainable strain hardening geopolymer composites, Cement Concr. Compos., 122 (2021) 104167.

[89] M. Maalej, V.C. Li, T. Hashida, Effect of fiber rupture on tensile properties of short fiber composites, J. Eng. Mech., 121 (1995) 903-913.

[90] V.C. Li, Y. Wang, S. Backer, A micromechanical model of tension-softening and bridging toughening of short random fiber reinforced brittle matrix composites, J. Mech. Phys. Solids., 39 (1991) 607-625.

[91] B.T. Huang, J.Q. Wu, J. Yu, J.G. Dai, C.K. Leung, High-strength seawater sea-sand Engineered Cementitious Composites (SS-ECC): Mechanical performance and probabilistic modelling, Cement Concr. Compos., 114 (2020) 103740.

[92] B.T. Huang, K.F. Weng, J. X, Y. Xiang, J.G. Dai, V.C. Li, Engineered/strain-hardening cementitious composites (ECC/SHCC) with an ultra-high compressive strength over 210 MPa, Compos. Commun., 26 (2021) 100775.

[93] K.Q. Yu, Y.C. Wang, J.T. Yu, S.L. Xu, A strain-hardening cementitious composites with the tensile capacity up to 8%, Constr. Build. Mater., 137 (2017) 410-419.

[94] G.P. van Zijl, V. Slowik, R.D. Toledo Filho, F.H. Wittmann, H. Mihashi, Comparative testing of

crack formation in strain-hardening cement-based composites (SHCC), Mater. Struct., 49 (2016) 1175-1189.

[95] V.C. Li, S. Wang, C. Wu, Tensile strain-hardening behavior of polyvinyl alcohol engineered cementitious composite (PVA-ECC), ACI Mater. J., 98 (6) (2001) 483-492.

[96] V.C. Li, C. Wu, S. Wang, A. Ogawa, T. Saito, Interface tailoring for strain-hardening polyvinyl alcohol-engineered cementitious composite (PVA-ECC), ACI Mater. J., 99 (5) (2002) 463-472.

[97] V.C. Li, S.X. Wang, Microstructure variability and macroscopic composite properties of high performance fiber reinforced cementitious composites, Probab. Eng. Mech., 21(3) (2006) 201-206.

[98] R. Moinia, A. Baghaie, F.B. Rodriguez, P.D. Zavattieri, J. P. Youngblood, J. Olek, Quantitative microstructural investigation of 3D-printed and cast cement pastes using micro-computed tomography and image analysis, Cement Concr. Res., 147 (2021) 106493.

[99] Y. Chen, K. Jansen, H.Z. Zhang, C.R. Rodriguez, Y.D. Gan, O. Çopuroğlu, E. Schlangen, Effect of printing parameters on interlayer bond strength of 3D printed limestone-calcined clay-based cementitious materials: An experimental and numerical study, Constr. Build. Mater., 262 (2020) 120094.

[100] A.V. Rahul, M. Santhanam, H. Meena, Z. Ghani, Effect of coarse aggregate volume on fracture behavior of self compacting concrete, Constr. Build. Mater., 52 (2014) 137-145.

[101] Z. Ge, A.M. Tawfek, H.Z. Zhang, Y.W. Yang, H.Q. Yuan, R.J. Sun, Z. Wang, Influence of an extrusion approach on the fiber orientation and mechanical properties of engineering cementitious composite, Constr. Build. Mater., 306 (2021) 124876.

[102] V.C. Li, C.K.Y. Leung, Steady-state and multiple cracking of short random fiber composites, J. Eng. Mech., 118 (1992) 2246-2264.

[103] T. Kanda, V.C. Li, Practical design criteria for saturated pseudo strain hardening behaviour in ECC, J. Adv. Concr. Technol., 4(1) (2006) 59-72.

[104] T. Kanda, V.C. Li, Multiple cracking sequence and saturation in fiber reinforced cementitious composites, Concr. Res. Technol., 9 (2) (1998) 19-33.

[105] Y.C. Wang, F.C. Liu, J.T. Yu, F.Y. Dong, J.H. Ye, Effect of polyethylene fiber content on physical and mechanical properties of engineered cementitious composites, Constr. Build. Mater., 251 (2020) 118917.

[106] T. Huang, Y.X. Zhang, Numerical modelling of mechanical behaviour of engineered cementitious composites under axial tension, Comput. Struct., 173 (2016) 95-108.

[107] G.A. Rao, Long-term drying shrinkage of mortar- influence of silica fume and size of fine aggregate, Cement Concr. Res., 31 (2001) 171-175.

[108] I.M. Nikbin, M.H.A. Beygi, M.T. Kazemi, J.V. Amiri, E. Rahmani, S. Rabbanifar, M. Eslami,

Effect of coarse aggregate volume on fracture behavior of self compacting concrete, Constr. Build. Mater., 52 (2014) 137-145.

[109] C.K. Leung, V.C. Li, First-cracking strength of short fiber-reinforced ceramics, Ceram. Eng. Sci. Proc., (1989) 1164-1178.

[110] Z.M. Wu, K.H. Khayat, C.J. Shi, Changes in rheology and mechanical properties of ultra-high performance concrete with silica fume content, Cement Concr. Res., 123 (2019) 105786.

[111] Z. Lin, T. Kanda, V.C. Li, On interface property characterization and performance of fiber reinforced cementitious composites, Concr. Sci. Eng., 1 (1999) 173-184.

[112] C. Ding, L.P. Guo, B. Chen, Theoretical analysis on optimal fiber-matrix interfacial bonding and corresponding fiber rupture effect for high ductility cementitious composites, Constr. Build. Mater., 223 (2019) 841-851.

[113] J.X. Li, J. Weng, Z.T. Chen, E.H. Yang, A generic model to determine crack spacing of short and randomly oriented polymeric fiber-reinforced strain-hardening cementitious composites (SHCC), Cement Concr. Compos., 118 (2021) 103919.

[114] E.H. Yang, S. Wang, Y. Yang, V.C. Li, Fiber-bridging constitutive law of engineered cementitious composites, J. Adv. Concr. Technol., 6 (1) (2008) 181-193.